

¹
² Susceptible host dynamics explain pathogen resilience to
³ perturbations

⁴
⁵ Sang Woo Park^{1,*} Bjarke Frost Nielsen² Emily Howerton² Bryan T. Grenfell^{2,3,4}
⁶ Sarah Cobey¹

⁷ **1** Department of Ecology and Evolution, University of Chicago, Chicago, IL, USA

⁸ **2** Department of Ecology and Evolutionary Biology, Princeton University,
Princeton, NJ, USA

¹⁰ **3** High Meadows Environmental Institute, Princeton University, Princeton, NJ,
USA

¹² **4** Princeton School of Public and International Affairs, Princeton, NJ, USA

¹³ *Corresponding author: swp2@uchicago.edu

¹⁴ **Abstract**

¹⁵ Interventions to slow the spread of SARS-CoV-2 significantly disrupted the transmission
¹⁶ of other pathogens. As interventions lifted, whether and when human pathogens
¹⁷ would eventually return to their pre-pandemic dynamics remains to be answered.
¹⁸ Here, we present a framework for estimating pathogen resilience based on how fast
¹⁹ epidemic patterns return to their pre-pandemic dynamics. By analyzing time series
²⁰ data from Hong Kong, Canada, Korea, and the US, we quantify the resilience of com-
²¹ mon respiratory pathogens and further predict when each pathogen will eventually
²² return to its pre-pandemic dynamics. Our predictions closely match the observed
²³ deviations (or lack thereof) from the pre-COVID dynamics and reveal long-term
²⁴ impacts of pandemic perturbations. We find a faster rate of susceptible replenish-
²⁵ ment underlies pathogen resilience and sensitivity to both large and small perturba-
²⁶ tions. Overall, our analysis highlights the persistent nature of common respiratory
²⁷ pathogens compared to vaccine-preventable infections, such as measles.

²⁸ **Significance Statement**

29 Introduction

30 Non-pharmaceutical interventions to slow the spread of SARS-CoV-2 disrupted the
 31 transmission of other human respiratory pathogens, adding uncertainties to their fu-
 32 ture epidemic dynamics and their public health burden [1]. As interventions lifted,
 33 large heterogeneities in outbreak dynamics were observed across different pathogens
 34 in different countries, with some pathogens exhibiting earlier and faster resurgences
 35 than others [2, 3, 4]. Heterogeneities in the overall reduction in transmission and the
 36 timing of re-emergence likely reflect differences in intervention patterns, pathogen
 37 characteristics, immigration/importation from other countries, and pre-pandemic
 38 pathogen dynamics [5]. Therefore, comparing the differential impact of the pandemic
 39 perturbations across pathogens can provide unique opportunities to learn about un-
 40 derlying pathogen characteristics across different populations, such as their trans-
 41 missibility or duration of immunity, from heterogeneities in re-emergence patterns
 42 [6].

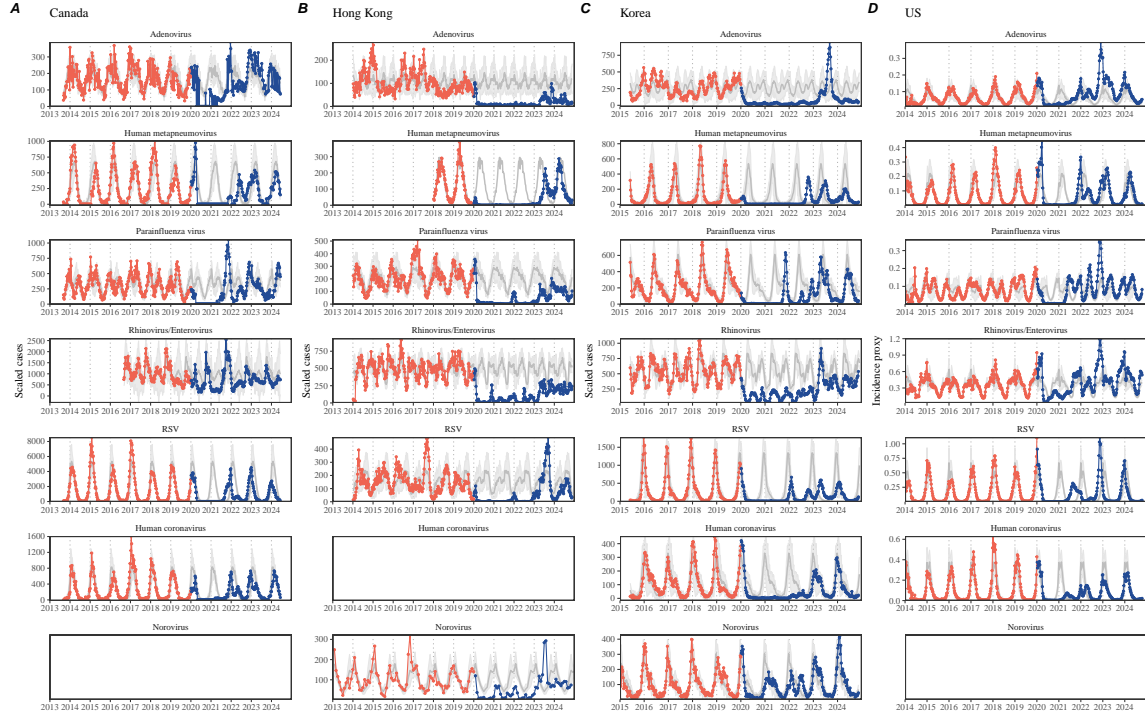


Figure 1: **Observed heterogeneity in responses to pandemic perturbations across respiratory pathogens and norovirus in (A) Canada, (B) Hong Kong, (C) Korea, and (D) US.** Red points and lines represent data before 2020. Blue points and lines represent data since 2020. Gray lines and shaded regions represent the mean seasonal patterns and corresponding 95% confidence intervals around the mean. Mean seasonal patterns were calculated by aggregating cases before 2020 into 52 weekly bins and taking the average in each week. Cases were scaled to account for changes in testing patterns (Materials and Methods).

43 Even though more than five years have passed since the emergence of SARS-CoV-
44 2, we still observe persistent changes in pathogen dynamics following the pandemic
45 perturbations. For example, compared to pre-pandemic, seasonal patterns, human
46 metapneumovirus in Korea seems to circulate at lower levels, whereas RSV in Ko-
47 rea seems to exhibit different seasonality (Figure 1). These observations suggest
48 the possibility of a long-term change in pathogen dynamics following the pandemic
49 perturbations, which might be driven by a long-term shift in human behavior or
50 population-level immunity [7, 8]. For example, the emergence of SARS-CoV-2 could
51 have caused a long-term shift in population-level immunity through its interactions
52 with other pathogens [9], especially with seasonal coronaviruses [7, 10, 11]. The pos-
53 sibility of a long-lasting impact of the pandemic perturbations poses an important
54 question for future infectious disease dynamics: can we predict whether and when
55 other pathogens will eventually return to their pre-pandemic dynamics?

56 So far, most analyses of respiratory pathogens after pandemic perturbations have
57 focused on characterizing the timing of rebound [1, 12, 5]. Instead, we seek to char-
58 acterize how fast (and whether) a pathogen returns to its pre-pandemic dynamics.
59 These two concepts have a subtle but important difference. For example, it took
60 more than 3 years for human metapneumovirus to rebound in Hong Kong, but the
61 observed epidemic patterns in 2024 appear similar to the pre-pandemic seasonal
62 mean, suggesting a possible return to pre-pandemic dynamics, though confirmation
63 may require multiple seasons (Figure 1). Measuring this rate of return is useful be-
64 cause it allows us to quantify the ecological resilience of a host-pathogen system,
65 which can inform responses to future interventions [13, 14, 15, 16].

66 In this study, we lay out theoretical and statistical approaches to characterizing
67 the resilience of a host-pathogen system based on how fast the system recovers from
68 perturbation. We begin by laying out a few representative scenarios that capture
69 the potential impact of pandemic perturbations on endemic pathogen dynamics and
70 illustrate how resilience can be measured by comparing the pre- and post-pandemic
71 dynamics of susceptible and infected hosts. In practice, information on susceptible
72 hosts is often unavailable, making this theoretical approach infeasible. Instead, we
73 utilize a mathematical technique to reconstruct attractors from the data [17], which
74 allows us to measure the rate at which the host-pathogen system approaches this
75 empirical attractor after a perturbation; we define this rate to be the empirical
76 resilience of the host-pathogen system. We use this method to analyze pathogen
77 surveillance data for respiratory and non-respiratory pathogens from Canada, Hong
78 Kong, Korea, and the US. Finally, we show that susceptible host dynamics explain
79 variation in pathogen resilience and demonstrate that more resilient pathogens will be
80 less sensitive to perturbations caused by demographic stochasticity, thereby providing
81 a direct link between pathogen resilience and persistence.

82 Conceptual introduction to pathogen resilience

83 In the classical ecological literature, the resilience of an ecological system is measured
84 by the rate at which the system returns to its reference state following a perturbation
85 [13, 14, 15, 16]. This rate corresponds to the largest real part of the eigenvalues of
86 the linearized system near equilibrium—here, we refer to this value as the *intrinsic*
87 resilience of the system, which represents the expected rate of return from perturbed
88 states. In practice, we rarely know the true model describing the dynamics of com-
89 mon respiratory pathogens, limiting our ability to infer the intrinsic resilience of a
90 system. Instead, we can measure the *empirical* resilience of a host-pathogen system
91 by looking at how fast the system returns to the pre-perturbation endemic dynamics
92 after the perturbation has ended. The COVID-19 pandemic provides a crucial exam-
93 ple of a major perturbation, providing unique opportunities to measure the resilience
94 of a host-pathogen system across different countries.

95 **Resilience of a single-strain system under a short-term perturbation.**
96 As an example, we begin with a simple Susceptible-Infected-Recovered-Susceptible
97 (SIRS) model with seasonally forced transmission and demography (i.e., birth and
98 death). The SIRS model is the simplest model that allows for the waning of immunity
99 and is commonly used for modeling the dynamics of respiratory pathogens [18]. First,
100 consider a pandemic perturbation that reduces transmission by 50% for 6 months
101 starting in 2020, which causes epidemic patterns to deviate from their original stable
102 annual cycle for a short period of time and eventually come back (Figure 2A). To
103 measure the resilience of this system empirically, we first need to be able to measure
104 the distance from its pre-pandemic attractor, which is defined as a set of points in
105 state space or phase plane that the system is pulled towards [19]. There are many
106 ways we can measure the distance from the attractor, but for illustrative purposes, we
107 choose one of the most parsimonious approaches: we look at how the susceptible (S)
108 and infected (I) populations change over time and measure the Euclidean distance on
109 the SI phase plane, using the counterfactual unperturbed phase plane as a reference
110 (Figure 2B; Materials and Methods). In this simple case, the locally estimated
111 scatterplot smoothing (LOESS) fit indicates that the distance from the attractor
112 decreases exponentially (linearly on a log scale) with time on average (Figure 2C).
113 Furthermore, the overall rate of return approximates the intrinsic resilience of the
114 seasonally unforced system (Figure 2C).

115 **Resilience of a single-strain system under a long-term perturbation.**
116 Alternatively, pandemic perturbations can have a lasting impact on the forces driv-
117 ing pathogen dynamics through a long-term reduction in transmission or permanent
118 change in immunity. As an example, we consider a scenario in which a 10% reduc-
119 tion in transmission persists even after the major pandemic perturbations are lifted
120 (Figure 2D–F). In such cases, we cannot know whether the pathogen will return to
121 its original cycle or a different cycle until many years have passed, and we cannot
122 a priori measure the distance to the new unknown attractor that the system might
123 eventually approach. Nonetheless, we can still measure the distance from the pre-

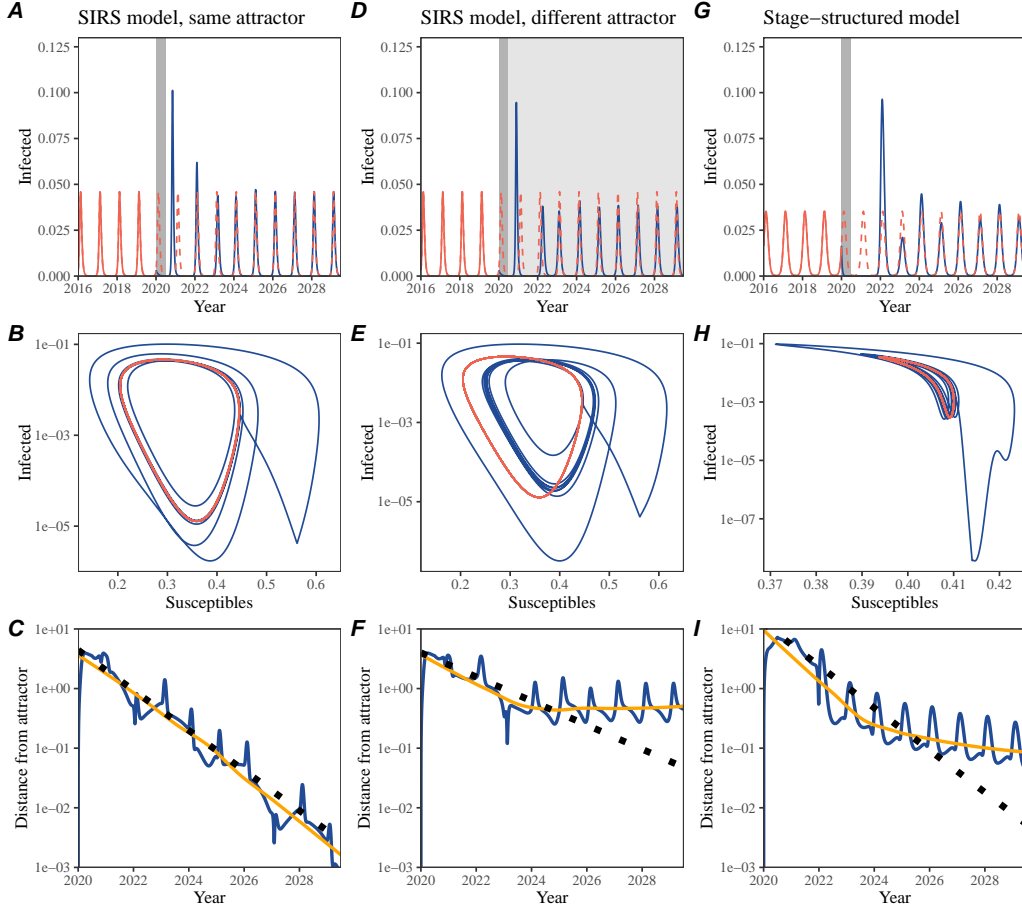


Figure 2: A simple method to measure pathogen resilience following pandemic perturbations across different scenarios. (A, D, G) Simulated epidemic trajectories across various models. Red and blue solid lines represent epidemic dynamics before and after pandemic perturbations are introduced, respectively. Red dashed lines represent counterfactual epidemic dynamics in the absence of perturbations. Gray regions indicate the duration of perturbations with the dark gray region representing a 50% transmission reduction and the light gray region representing a 10% transmission reduction. (B, E, H) Phase plane representation of the time series in panels A, D, and G alongside the corresponding susceptible host dynamics. Red and blue solid lines represent epidemic trajectories on an SI phase plane before and after perturbations are introduced, respectively. (C, F, I) Changes in distance from the attractor over time on a log scale. Blue lines represent the distance from the attractor. Orange lines represent the locally estimated scatterplot smoothing (LOESS) fits to the logged distance from the attractor. Dotted lines show the intrinsic resilience of the seasonally unforced system.

124 pandemic attractor and ask how the distance changes over time (Figure 2E). The
125 LOESS fit suggests that the distance from the pre-pandemic attractor will initially
126 decrease exponentially on average (equivalently, linearly on a log scale) and even-
127 tually plateau (Figure 2F). Here, a permanent 10% reduction in transmission rate
128 slows the system, which causes the distance from the pre-pandemic attractor initially
129 to decrease at a slower rate (Figure 2F) than it would have otherwise (Figure 2C)
130 before plateauing at a fixed distance between the two attractors. This example shows
131 that resilience is not necessarily an intrinsic property of a specific pathogen. Instead,
132 pathogen resilience is a property of a specific attractor that a host-pathogen system
133 approaches, which depends on both pathogen and host characteristics.

134 **Resilience of a single-strain system with long-term transients.** Finally,
135 transient phenomena can further complicate the picture (Figure 2G–I). For exam-
136 ple, a stage-structured model that accounts for reduction in secondary susceptibility
137 initially exhibits a stable annual cycle, but perturbations from a 10% reduction in
138 transmission for 6 months cause the epidemic to shift to biennial cycles (Figure 2G).
139 The system eventually approaches the original pre-pandemic attractor (Figure 2H),
140 suggesting that this biennial cycle is a transient. The LOESS fit indicates that the
141 distance from the attractor initially decreases exponentially at a rate that is consis-
142 tent with the intrinsic resilience of the seasonally unforced stage-structured system,
143 but the approach to the attractor slows down with the damped oscillations (Figure
144 2I). This behavior is also referred to as a ghost attractor, which causes long tran-
145 sient dynamics and slow transitions [20]. Strong seasonal forcing in transmission can
146 also lead to transient phenomena for a simple SIRS model, causing a slow return to
147 pre-perturbation dynamics (Supplementary Figure S1).

148 **Resilience of a two-strain system.** This empirical approach allows us to
149 measure the resilience of a two-strain host-pathogen system as well even when we
150 have incomplete observation of the infection dynamics. Simulations from a simple
151 two-strain competition system illustrate that separate analyses of individual strain
152 dynamics (e.g., RSV subtype A vs B) and a joint analysis of total infections (e.g.,
153 total RSV infections) yield identical resilience estimates (Supplementary Figure S2,
154 3). This is expected because eigenvalues determine the dynamics of the entire system
155 around the equilibrium, meaning that both strains should exhibit identical rates of
156 return following a perturbation. Analogous to a single-strain system, strong sea-
157 sonal forcing in transmission can cause the two-strain system to slow down through
158 transient phenomena (Supplementary Figure S4).

159 These observations yield three insights. First, we can directly estimate the empi-
160rical resilience of a host-pathogen system by measuring the rate at which the system
161 approaches an attractor, provided that we have a way to quantify the distance from
162 the attractor—as we discuss later, the attractor of a system can be reconstructed
163 from data from mathematical theory without making assumptions about the under-
164lying model. The empirical approach to estimating pathogen resilience is particularly
165convenient because it does not require us to know the true underlying model; esti-
166mating the intrinsic resilience from fitting misspecified models can lead to biased

estimates (Supplementary Figure S5). Second, resilience estimates allow us to make phenomenological predictions about the dynamics of a host-pathogen system following a perturbation. Assuming that an attractor has not changed and the distance from the attractor will decrease exponentially over time, we can estimate when the system should reach an attractor. Finally, a change in the (exponential) rate of approach can provide information about whether the system has reached an alternative attractor, or a ghost attractor, that is different from the original, pre-pandemic attractor. These alternative attractors may reflect permanent changes in transmission patterns as well as changes in immune landscapes. There will be periods of time when it is difficult to tell whether pathogen dynamics are still diverging from the original attractor due to a long-term perturbation, or have entered the basin of attraction of a new attractor. Now that several years have passed since major interventions have been lifted, many respiratory pathogens may have had sufficient time to begin returning to their post-intervention attractors—empirical comparisons between current cases and pre-pandemic cases are consistent with this hypothesis (Figure 1). With recent data, we can start to evaluate whether we see early signs of convergence to the former attractor or a new one.

Inferring pathogen resilience from real data

Based on these patterns, we now lay out our approach to estimating pathogen resilience from real data (Figure 3). We first tested this approach against simulations and applied it to real data. Specifically, we analyzed case time series of respiratory pathogens from four countries: Canada, Hong Kong, Korea, and the US.

So far, we have focused on simple examples that assume a constant transmission reduction during the pandemic. However, in practice, the impact of pandemic perturbations on pathogen transmission is likely more complex (Figure 3A), reflecting the introduction and relaxation of various intervention strategies. In some cases, strong perturbations likely caused local fadeouts, requiring immigration/importation from another location for epidemic rebound. Such complexities could lead to longer delays between the introduction of pandemic perturbations and pathogen rebound as well as temporal variation in outbreak sizes (Figure 3B); in this example, continued transmission reduction from interventions limits the size of the first outbreak in 2021 following the rebound, allowing for a larger outbreak in 2022 when interventions are further relaxed.

Previously, we relied on the dynamics of susceptible and infected hosts to compute the distance from the attractor (Figure 2), but information on susceptible hosts is rarely available in practice. In addition, uncertainties in case counts due to observation error, strain evolution, and multiannual cycles in the observed epidemic dynamics (e.g., adenovirus circulation patterns in Hong Kong and Korea) add challenges to defining pre-pandemic attractors, which limits our ability to measure the distance from the attractor. To address these challenges, we can reconstruct an em-

207 empirical attractor by utilizing Takens' theorem [17], which states that an attractor of a
208 nonlinear multidimensional system can be mapped onto a delayed embedding (Materials
209 and Methods). For example, we can use delayed logged values of pre-pandemic
210 cases $C(t)$ (Figure 3C) to reconstruct the attractor:

$$\langle \log(C(t) + 1), \log(C(t - \tau) + 1), \dots, \log(C(t - (M - 1)\tau) + 1) \rangle, \quad (1)$$

211 where the delay τ and embedding dimension M are determined based on autocor-
212 relations and false nearest neighbors, respectively [21, 22]. This allows us to define
213 the pre-pandemic attractor as a points on an M -dimensional space. We can then
214 apply the same delay and embedding dimensions to the entire time series to deter-
215 mine the position in multi-dimensional state space (Figure 3D), which allows us to
216 measure the nearest neighbor distance between the current state of the system and
217 the empirical pre-pandemic attractor (Figure 3E). Specifically, the nearest neighbor
218 distance is calculated by computing the distance between the current position on
219 the M -dimensional space and all points in the empirical attractor set and taking the
220 minimum value. In theory, we can now quantify how fast this distance decreases by
221 fitting a linear regression on a log scale, where the slope of the linear regression em-
222 pirically measures pathogen resilience, with a steeper slope corresponding to a higher
223 resilience estimate (Figure 3E). However, resulting estimates of pathogen resilience
224 can be sensitive to choices about embedding delays and dimensions. For example,
225 using longer delays and higher dimensions tends to smooth out temporal variations
226 in the distance from the attractor (Supplementary Figure S6).

227 Complex changes in the distance from the attractor suggest that estimating
228 pathogen resilience from linear regression will be particularly sensitive to our choice
229 of fitting windows for the regression (Figure 3E). Therefore, before we tried estimat-
230 ing resilience from real data, we explored an automated window selection criteria
231 for linear regression and tested it against randomized, stochastic simulations across
232 a range of realistic pandemic perturbation shapes. In doing so, we also explored
233 optimal choices for embedding dimensions and evaluated our choices of fitting win-
234 dow parameters and embedding dimensions by quantifying correlation coefficients
235 between the estimated resilience and the intrinsic resilience of a seasonally unforced
236 system (Materials and Methods). Overall, we found large variation in estimation
237 performances with correlation coefficients ranging from 0.21 to 0.61 (Supplementary
238 Figure S7). In almost all cases, the automated window selection approach outper-
239 formed a naive approach, which performs regression using all data from the the
240 timing of peak distance to current time (Supplementary Figure S7).

241 Based on the best-performing window selection criteria and embedding dimen-
242 sion, we applied this approach to pathogen surveillance data presented in Figure
243 1 (Materials and Methods). For each time series, we applied Takens' theorem in-
244 dependently to reconstruct the empirical attractor and obtained the corresponding
245 time series of distances from attractors (Supplementary Figure S8). Then, we used
246 the automated window selection criteria to fit a linear regression and estimated the
247 empirical resilience for each pathogen in each country (Supplementary Figure S8);

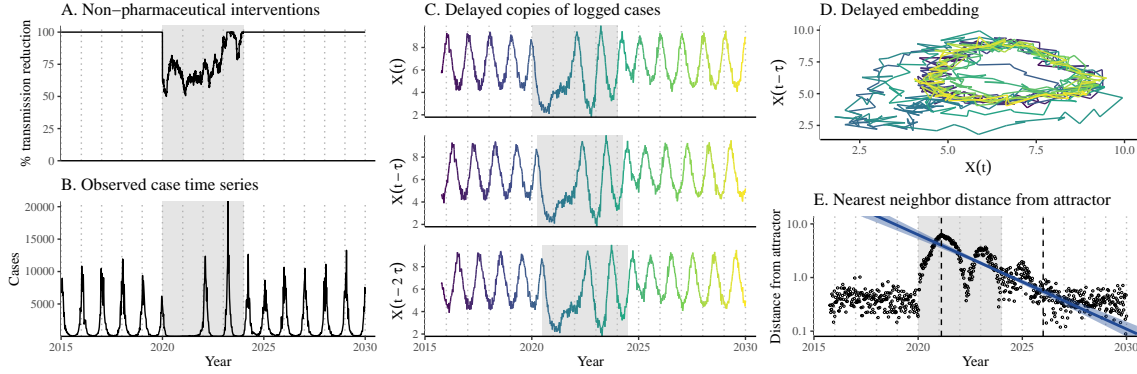


Figure 3: **A schematic diagram explaining the inference of pathogen resilience from synthetic data.** (A) A realistic example of simulated pandemic perturbations, represented by a relative reduction in transmission. (B) The impact of the synthetic pandemic perturbation on epidemic dynamics simulated using a SIRS model with demographic stochasticity. (C) Generating delayed copies of the logged time series allows us to obtain an embedding. (D) Two dimensional representation of an embedding. (E) Delayed embedding allows us to calculate the nearest neighbor distance from the empirical attractor, which is determined based on the pre-pandemic time series. Blue lines and dashed regions represent the linear regression fit and the associated 95% confidence interval. This distance time series can be used to infer pathogen resilience after choosing an appropriate window for linear regression. For illustration purposes, an arbitrary fitting window was chosen.

the window selection criteria gave poor regression windows in three cases (norovirus in Hong Kong and Korea and rhinovirus/enterovirus in the US), leading to unrealistically low resilience estimates, and so we used ad-hoc regression windows instead (Supplementary Figure S9; Materials and Methods).

For all pathogens we considered, resilience estimates fall between 0.4/year and 1.8/year (Figure 4A). We estimated the mean resilience of common respiratory pathogens to be 0.99/year (95% CI: 0.81/year–1.18/year). For reference, this is ≈ 7.5 times higher than the intrinsic resilience of pre-vaccination measles in England and Wales ($\approx 0.13/\text{year}$). Finally, resilience estimates for norovirus, a gastrointestinal pathogen, were comparable to those of common respiratory pathogens: 1.44/year (95% CI: 1.01/year–1.87/year) for Hong Kong and 1.07/year (95% CI: 0.86/year–1.29/year) for Korea. Based on a simple ANOVA test, we did not find significant differences in resilience estimates across countries ($p = 0.25$) or pathogens ($p = 0.67$).

Using resilience estimates, we predicted when each pathogen would hypothetically return to their pre-pandemic dynamics, assuming no long-term change in the attractor. Specifically, we extended our linear regression fits to distance-from-attractor time series and ask when the predicted regression line will cross a threshold value; since we relied on nearest neighbor distances, pre-pandemic distances are always greater than zero (Figure 3E), meaning that we can use the mean of pre-pandemic

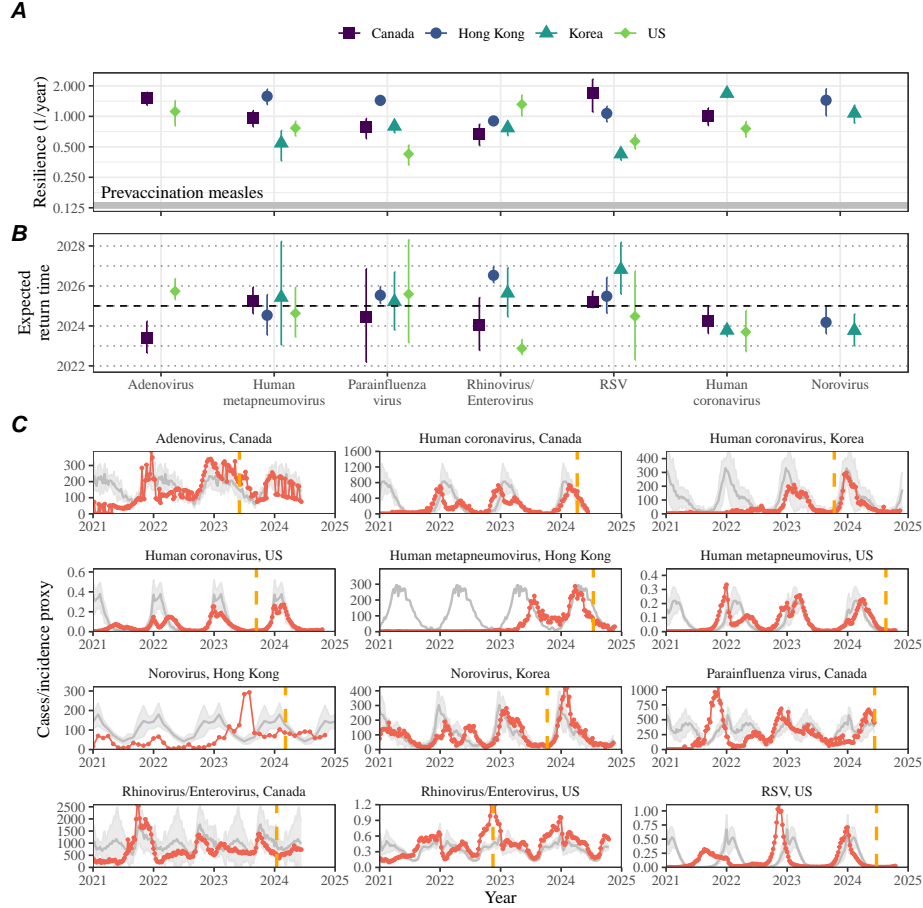


Figure 4: Summary of resilience estimates and predictions for return time. (A) Estimated pathogen resilience. The gray horizontal line represents the intrinsic resilience of pre-vaccination measles dynamics. (B) Predicted timing of when each pathogen will return to their pre-pandemic cycles. The dashed line in panel B indicates the end of 2024. Error bars represent 95% confidence intervals. (C) Observed dynamics for pathogen that are predicted to have returned before the end of 2024. Red points and lines represent data before 2020. Gray lines and shaded regions represent the mean seasonal patterns and corresponding 95% confidence intervals around the mean, previously shown in Figure 1. Orange vertical lines represent the predicted timing of return.

267 distances as our threshold.

268 We predicted that a return to pre-pandemic cycles has occurred or would be
 269 imminent for most pathogens (Figure 4B). In particular, we predicted that 12 out
 270 of 23 pathogen-country pairs should have already returned before the end of 2024.
 271 For almost all pathogens that were predicted to have returned already, the observed
 272 epidemic dynamics showed clear convergence towards their pre-pandemic seasonal

averages, confirming our predictions (Figure 4C). However, there were a few exceptions, including norovirus in Hong Kong and rhinovirus/enterovirus in the US, where the observed epidemic dynamics in 2024 exhibit clear deviation from their pre-pandemic seasonal averages (Figure 4C; Figure S9). These observations suggest a possibility that some common respiratory pathogens may have converged to different attractors or are still exhibiting non-equilibrium dynamics. In contrast, pathogens that were predicted to have not returned yet also showed clear differences from their pre-pandemic seasonal averages; as many of these pathogens are predicted to return in 2025–2026, we may be able to test these predictions in near future (Supplementary Figure S10). Our reconstructions of distance time series and estimates of pathogen resilience and expected return time were generally robust to choices of embedding dimensions (Supplementary Figure S11–12).

Susceptible host dynamics explain variation in pathogen resilience

So far, we have focused on quantifying pathogen resilience from the observed patterns of pathogen re-emergence following pandemic perturbations. But what factors determine the resilience of a host-pathogen system? To address this question, we used the SIRS model to explore how changes in susceptible host dynamics affect pathogen resilience. To do so, we varied the basic reproduction number \mathcal{R}_0 , which represents the average number of secondary infections caused by a newly infected individual in a fully susceptible population, and the duration of immunity and computed intrinsic resilience for each parameter.

We found that an increase in \mathcal{R}_0 and a decrease in the duration of immunity correspond to an increase in pathogen resilience (Figure 5A). Similarly, an increase in \mathcal{R}_0 and a decrease in the duration of immunity corresponds to a faster per-capita rate of susceptible replenishment, which is defined as the ratio between absolute rate at which new susceptibles enter the population and the equilibrium number of susceptible individuals in the population, S^* (Figure 5B). We note that a higher \mathcal{R}_0 drives a faster per-capita susceptible replenishment rate by decreasing the susceptible proportion at equilibrium, S^* . For a simple SIR model that assumes a life-long immunity, we can show analytically that pathogen resilience is proportional to the per-capita rate of susceptible replenishment (Materials and Methods). Overall, these observations suggest that a faster per-capita susceptible replenishment rate causes the system to be more resilient.

By taking the average values of empirical resilience for each pathogen, we were able to map each pathogen onto a set of parameters of the SIRS model that are consistent with corresponding resilience estimates (Figure 5A). Across all pathogens we considered, we estimated that the average duration of immunity is likely to be short (< 4 years) across a plausible range of \mathcal{R}_0 (< 6). We were also able to obtain a plausible range of susceptible replenishment rates for each pathogen (Figure 5B),

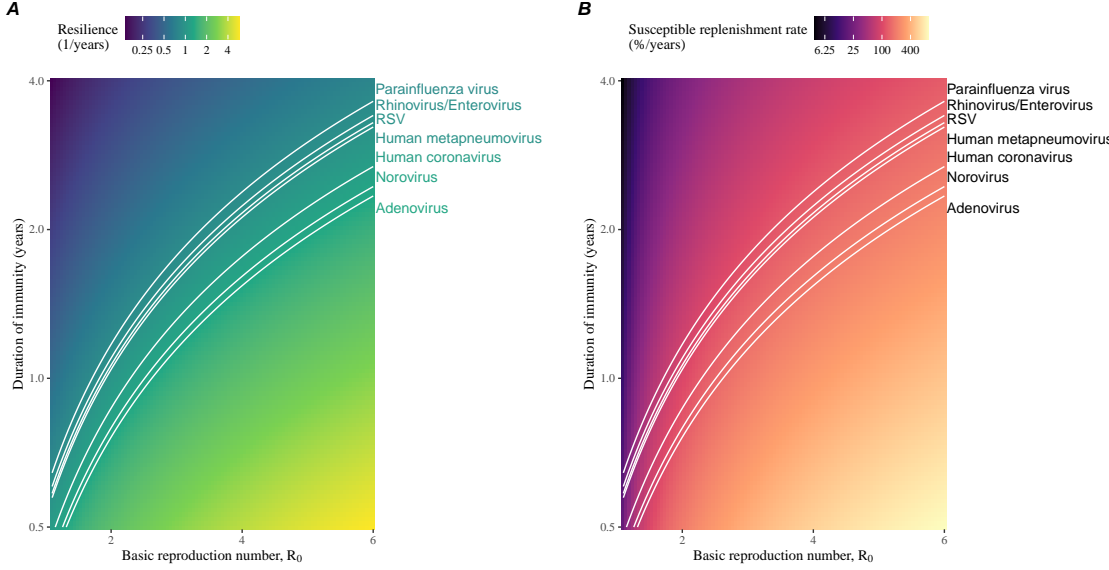


Figure 5: Linking pathogen resilience to epidemiological parameters and susceptible host dynamics. (A) Intrinsic resilience as a function of the basic reproduction number \mathcal{R}_0 and the duration of immunity. (B) Per-capita susceptible replenishment rate as a function of the basic reproduction number \mathcal{R}_0 and the duration of immunity. The standard SIRS model without seasonal forcing is used to compute intrinsic resilience and the per-capita susceptible replenishment rate. Lines correspond to a set of parameters that are consistent with mean resilience estimates for each pathogen, averaged across different countries.

313 but there was a large uncertainty in the estimates for susceptible replenishment rates
314 due to a lack of one-to-one correspondence between susceptible replenishment rates
315 and pathogen resilience.

316 **Pathogen resilience determines sensitivity to stochastic perturbations**

318 Even in the absence of major pandemic perturbations, host-pathogen systems are
319 expected to experience continued perturbations of varying degrees from changes in
320 epidemiological conditions, such as human behavior, climate, and viral evolution.
321 These perturbations can also arise from demographic stochasticity, which is inher-
322 ent to any ecological system. Here, we used a seasonally unforced SIRS model with
323 constant birth and death rates to explore how resilience of a host-pathogen sys-
324 tem determines the sensitivity to perturbations caused by demographic stochasticity
325 (Materials and Methods).

326 We found that resilience of a host-pathogen system determines the amount of de-

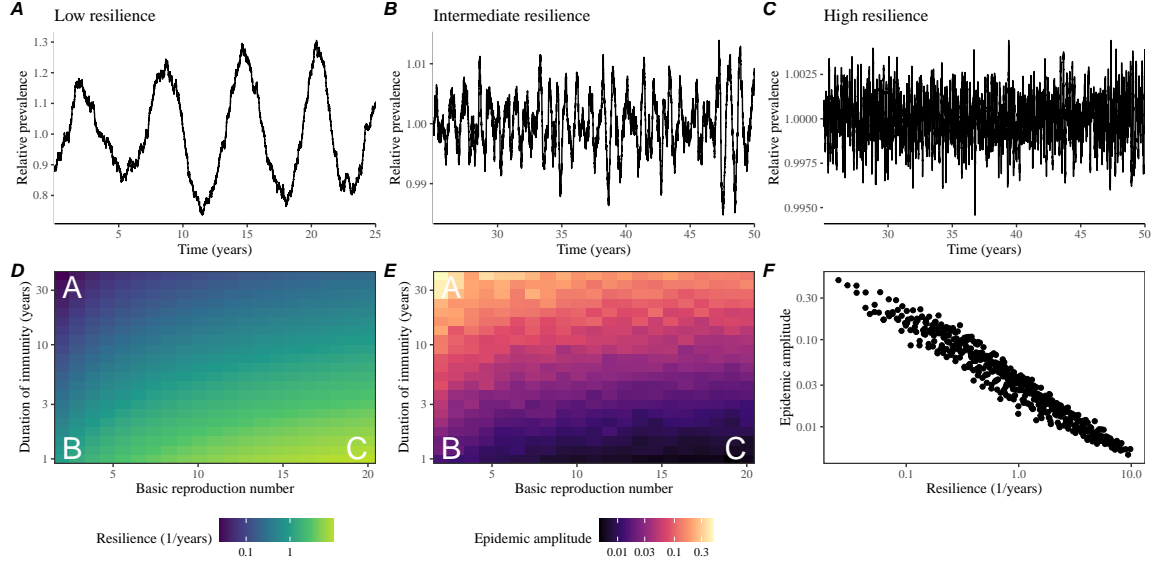


Figure 6: Linking resilience of a host-pathogen system to its sensitivity to stochastic perturbations. (A–C) Epidemic trajectories of a stochastic SIRS model across three different resilience values: low, intermediate, and high. The relative prevalence was calculated by dividing infection prevalence by its mean value. (D) Intrinsic resilience of a system as a function of the basic reproduction number \mathcal{R}_0 and the duration of immunity. (E) Epidemic amplitude as a function of the basic reproduction number \mathcal{R}_0 and the duration of immunity. The epidemic amplitude corresponds to $(\max I - \min I)/(2\bar{I})$, where \bar{I} represents the mean prevalence. Labels A–C in panels D and E correspond to scenarios shown in panels A–C. (F) The relationship between pathogen resilience and epidemic amplitude.

327 deviation from the deterministic trajectory caused by demographic stochasticity, with
 328 less resilient systems experiencing larger deviations (Figure 6). Notably, less resilient
 329 systems also exhibited slower epidemic cycles (Figure 6A–C). The periodicity of this
 330 epidemic cycle matched those predicted by the intrinsic periodicity of the system
 331 (Supplementary Figure S13) where the intrinsic resilience of the system is inversely
 332 proportional to its intrinsic periodicity (Supplementary Figure S14). However, we
 333 note that the interplay between seasonal transmission and intrinsic periodicity can
 334 also lead to complex cycles, as illustrated by a recent analysis of *Mycoplasma pneumoniae*
 335 dynamics [23].

336 We also note that the intrinsic resilience is not the sole determinant for how sen-
 337 sitive the system is to stochastic perturbations. For example, the population size
 338 and average duration of infection also affect the amount of deviation from the deter-
 339 ministic trajectory caused by demographic stochasticity, even though these quantities
 340 have little to no impact on the intrinsic resilience (Supplementary Figure S15). These
 341 conclusions were robust for the seasonally forced SIRS model (Supplementary Figure

342 S16).

343 Discussion

344 COVID-19 pandemic interventions caused major disruptions to circulation patterns
345 of both respiratory and non-respiratory pathogens, adding challenges to predicting
346 their future dynamics [1, 2, 3, 4]. However, these perturbations offer large-scale natural
347 experiments for understanding how different pathogens respond to perturbations.
348 In this study, we showed that pathogen re-emergence patterns following pandemic
349 perturbations can be characterized through the lens of ecological resilience and pre-
350 sented a new method for estimating pathogen resilience from time series data. We
351 showed that variation in pathogen resilience can be explained by the differences in
352 susceptible host dynamics, where faster replenishment of the susceptible pool corre-
353 sponds to a more resilient host-pathogen system. Finally, we showed that pathogen
354 resilience also determines the sensitivity to stochastic perturbations.

355 We analyzed case time series of common respiratory infections and norovirus
356 infections from Canada, Hong Kong, Korea, and the US to estimate their resilience.
357 Overall, we estimated the resilience of these pathogens to range from 0.4/year to
358 1.8/year, which is 3–14 times more resilient than prevaccination measles. Consistent
359 with other epidemiological evidence [24, 25, 26, 27], these resilience estimates indicate
360 that common respiratory pathogens and norovirus likely exhibit faster susceptible
361 replenishment and are therefore more persistent, indicating potential challenges in
362 controlling these pathogens.

363 Based on our resilience estimates, we made phenomenological predictions about
364 when each pathogen will return to their endemic cycles. For the most part, we
365 accurately predicted which pathogens should have already returned before the end
366 of 2024. However, there were two main exceptions (i.e., norovirus in Hong Kong
367 and rhinovirus/enterovirus in the US), suggesting that these pathogens may be con-
368 verging to new endemic cycles or experiencing long-term transient behavior. These
369 changes may reflect changes in surveillance or actual shift in the dynamics, caused
370 by permanent changes in behavior or population-level immunity. While it may seem
371 unlikely that permanent changes in behavior would only affect a few pathogens and
372 not others, we cannot rule out this possibility given differences in the observed mean
373 age of infections and therefore the differences in age groups that primarily drive
374 transmission [28, 29]. Differences in the mode of transmission between respiratory
375 vs gastrointestinal pathogens may also contribute to the differences in responses to
376 pandemic perturbations.

377 For almost half of the pathogens we considered, we predicted that their return
378 to original epidemic patterns is imminent. We will need a few more years of data
379 to test whether these pathogens will eventually return to their original dynamics or
380 eventually converge to a different attractor. We also cannot rule out the possibility
381 that some pathogens may exhibit long-term transient behaviors following pandemic

382 perturbations. Overall, these observations echo earlier studies that highlighted the
383 long-lasting impact of pandemic perturbations [8, 30, 31, 4, 23].

384 We showed that susceptible host dynamics shape pathogen resilience, where faster
385 replenishment of the susceptible population causes the pathogen to be more resilient.
386 For simplicity, we focused on waning immunity and birth as the main drivers of the
387 susceptible host dynamics but other mechanisms can also contribute to the replen-
388 ishment of the susceptible population. In particular, pathogen evolution, especially
389 the emergence of antigenically novel strains, can cause effective waning of immunity
390 in the population; therefore, we hypothesize that the rate of antigenic evolution is
391 likely a key feature of pathogen resilience. Future studies should explore the relation-
392 ship between the rate of evolution and resilience for antigenically evolving pathogens.
393 This result also highlights the importance of detailed measurements of changes in the
394 susceptible population through immune assays for understanding pathogen dynamics
395 [32].

396 Quantifying pathogen resilience also offers novel approaches to validating population-
397 level epidemiological models. So far, most model validation in infectious disease ecol-
398 ogy is based on the ability of a model to reproduce the observed epidemic dynamics
399 and to predict future dynamics [33, 34, 26, 35, 36]. However, many models can
400 perform similarly under these criteria. For example, two major RSV models have
401 been proposed to explain biennial epidemic patterns: (1) a stage- and age-structured
402 model that allows disease severity to vary with number of past infections and age of
403 infection [26] and (2) a pathogen-interaction model that accounts for cross immunity
404 between RSV and human metapneumovirus [34]. Since both models can accurately
405 reproduce the observed epidemic patterns, standard criteria for model validation
406 do not allow us to distinguish between these two models from population-level data
407 alone. Instead, it would be possible to measure the empirical resilience of each model
408 by simulating various perturbations and comparing the simulations to estimates of
409 empirical resilience from data, using pandemic perturbations as a reference.

410 There are several limitations to our work. First, we did not extensively explore
411 other approaches to reconstructing the attractor. Recent studies showed that more
412 sophisticated approaches, such as using non-uniform embedding, can provide more
413 robust reconstruction for noisy data [22]. In the context of causal inference, choices
414 about embedding can have major impact on the resulting inference [37]. Our re-
415 silience estimates are likely overly confident given a lack of uncertainties in attractor
416 reconstruction as well as the simplicity of our statistical framework. Nonetheless,
417 as illustrated in our sensitivity analyses, inferences about pathogen resilience in our
418 SIRS model appear to be robust to decisions about embedding lags and dimensions—
419 this is because tracking the rate at which the system approaches the attractor is likely
420 a much simpler problem than making inferences about causal directionality. Short
421 pre-pandemic time series also limit our ability to accurately reconstruct the attrac-
422 tor and contribute to the crudeness of our resilience estimates; although this is less
423 likely a problem for respiratory pathogens that are strongly annual, our attractor
424 reconstruction may be inaccurate for those exhibiting multi-annual cycles, such as

425 adenovirus in Hong Kong and Korea. Our framework also does not allow us to dis-
426 tinguish whether a system has settled to a new attractor or is experiencing long-term
427 transient behavior. Uncertainties in pathogen dynamics due to changes in testing
428 patterns further contribute to the crudeness of our resilience estimates.

429 While attractor reconstruction allows us to make model-free inferences of pathogen
430 resilience, it does not allow us to tease apart how different mechanisms contribute
431 to the resilience a host-pathogen system. Using the simple SIRS model, we illus-
432 trated that susceptible host dynamics are key determinants of pathogen resilience,
433 but we also found that there isn't a one-to-one correspondence between per capita
434 replenishment rate of the susceptible population and pathogen resilience estimates.
435 Future studies should explore using mechanistic models to explain heterogeneity in
436 resilience estimates across different pathogens.

437 Finally, our simulation-based analyses primarily focused on single-strain systems,
438 but real-world pathogens can interact with other pathogens, which can result in com-
439 plex dynamics [38, 39]. To address this limitation, we considered a simple model of
440 two competing strains (via cross immunity) and showed that the resilience of a cou-
441 pled system can be measured by studying the dynamics of either strain. However, this
442 conclusion likely depends on the strength and mechanism of strain interactions. For
443 example, ecological interference between two unrelated pathogens [38] will likely gen-
444 erate weaker coupling than cross-immunity between related pathogens; in the former
445 case, we do not necessarily expect two unrelated pathogens to have same resilience
446 despite their ecological interference. Some pathogen strains can also exhibit positive
447 interactions where infection by one strain can lead to an increased transmission of
448 another competing strain. For example, previous studies showed that an increased
449 dengue transmission through antibody-dependent enhancement can permit coexis-
450 tence and persistence of competing strains [40]; since pathogen transmissibility is a
451 major determinant of pathogen resilience, we tentatively hypothesize that positive
452 interactions such as antibody-dependent enhancement may increase the resilience of
453 a system. Future studies should explore how different mechanisms of pathogen inter-
454 actions contribute to the resilience of each competing pathogen as well as the entire
455 system. Despite these limitations, our study illustrates that quantifying pathogen
456 resilience can provide novel insights into pathogen dynamics. Furthermore, our qual-
457 itative prediction that common respiratory pathogens are more resilient than pre-
458 vaccination measles is also likely to be robust, given how rapidly many respiratory
459 pathogens returned to their original cycles following pandemic perturbations.

460 Predicting the impact of anthropogenic changes on infectious disease dynamics
461 is a fundamental aim of infectious disease research in a rapidly changing world. Our
462 study illustrates that how a host-pathogen system responds to both small and large
463 perturbations is largely predictable through the lens of ecological resilience. In par-
464 ticular, quantifying the resilience of a host-pathogen system offers a unique insight
465 into questions about endemic pathogens' responses to pandemic perturbations, in-
466 cluding whether some pathogens will exhibit long-lasting impact from the pandemic
467 perturbation or not. More broadly, a detailed understanding of the determinants of

468 pathogen resilience can provide deeper understanding of pathogen persistence.

469 Materials and Methods

470 Data

471 We gathered time series on respiratory infections from Canada, Hong Kong, Korea,
472 and United States (US). As a reference, we also included time series data on norovirus
473 infections when available. In contrast to respiratory pathogens, we hypothesized
474 gastrointestinal viruses, such as norovirus, to be differently affected by pandemic
475 perturbations.

476 Weekly time series of respiratory infection cases in Canada came from a publicly
477 available website by the Respiratory Virus Detection Surveillance System, which
478 collects data from select laboratories across Canada [41]. Weekly time series of
479 respiratory infection cases in Hong Kong came from a publicly available website
480 by the Centre for Health Protection, Department of Health [42, 43]. Weekly time
481 series of acute respiratory infection cases in Korea came from a publicly available
482 website by the Korea Disease Control and Prevention Agency [44]. Finally, weekly
483 time series of respiratory infection cases in the US were obtained from the National
484 Respiratory and Enteric Virus Surveillance System (NREVSS). Readers can request
485 the data from NREVSS at nrevss@cdc.gov. Time series on number of tests were also
486 available in Canada, Hong Kong, and the US, but not in Korea.

487 Data processing

488 For all time series, we rounded every year to 52 weeks by taking the average number
489 of cases and tests between the 52nd and 53rd week. We also rescaled all time series to
490 account for changes in testing patterns, which were then used for the actual analysis.

491 For Canada, an increase in testing was observed from 2013 to 2024 (Supplementary
492 Figure S17). To account for this increase, we calculated a 2 year moving average
493 for the number of tests for each pathogen, which we used as a proxy for testing effort.
494 Then, we divided the smoothed testing patterns by the smoothed value at the final
495 week such that the testing effort has a maximum of 1. We then divided weekly cases
496 by the testing effort to obtain a scaled case time series. A similar approach was used
497 earlier for an analysis of RSV time series in the US to account for changes in testing
498 patterns [26].

499 For Hong Kong, we applied the same scaling procedure to the time series as we
500 did for Canada. In this case, we only adjusted for testing efforts up to the end of 2019
501 because there was a major reduction in testing for common respiratory pathogens
502 between 2020 and 2023 (Supplementary Figure S18).

503 For Korea, while we did not have information on testing, the reported number
504 of respiratory infections consistently increased from 2013 to the end of 2019, which
505 we interpreted as changes in testing patterns (Supplementary Figure S19). Since

506 we did not have testing numbers, we used the weekly sum of all acute respiratory
507 viral infection cases as a proxy for testing, which were further smoothed with moving
508 average and scaled to have a maximum of 1. For Korea, we also only adjusted for
509 testing efforts up to the end of 2019.

510 In the US, there has been a large increase in testing for some respiratory pathogens,
511 especially RSV, which could not be corrected by simple scaling (Supplementary Fig-
512 ure S20). Instead, we derived an incidence proxy by multiplying the test positivity
513 with influenza-like illness positivity, which was taken from [https://gis.cdc.gov/
514 grasp/fluvview/fluportaldashboard.html](https://gis.cdc.gov/grasp/fluvview/fluportaldashboard.html). This method of estimating an inci-
515 dence proxy has been recently applied in the analysis of seasonal coronaviruses [7]
516 and *Mycoplasma pneumoniae* infections [4]. Detailed assumptions and justifications
517 are provided in [45].

518 Data summary

519 To make qualitative comparisons between pre- and post-perturbation dynamics of
520 respiratory pathogen circulation patterns, we calculated the mean seasonal patterns
521 using time series of either rescaled cases or incidence proxy estimates before 2020. We
522 did so by taking the mean value in each week across all years before 2020. Confidence
523 intervals around the means were calculated using a simple t test.

524 Estimating pathogen resilience

525 In order to measure pathogen resilience from surveillance data, we first reconstructed
526 the empirical pre-pandemic attractor of the system using Takens' embedding theorem
527 [17]. Specifically, for a given pathogen, we took the pre-pandemic (before 2020) case
528 time series $C(t)$ and reconstructed the attractor using delayed embedding with a
529 uniform delay of τ and dimension M :

$$X_{\tau,m}(t) = \langle \log(C(t) + 1), \log(C(t - \tau) + 1), \dots, \log(C(t - (M - 1)\tau) + 1) \rangle. \quad (2)$$

530 Here, the delay τ was determined by calculating the autocorrelation of the logged
531 pre-pandemic time series and asking when the autocorrelation crosses 0 for the first
532 time [22]; a typical delay for an annual outbreak is around 13 weeks.

533 Then, for a given delay τ , we determined the embedding dimension M using the
534 false nearest neighbors approach [21, 22]. To do so, we started with an embedding
535 dimension e and constructed a set of points $A_{\tau,e} = \{X_{\tau,e}(t) | t < 2020\}$. Then, for
536 each point $X_{\tau,e}(t)$, we determined the nearest neighbor from the set $A_{\tau,e}$, which we
537 denote $X_{\tau,e}(t_{nn})$ for $t \neq t_{nn}$. Then, if the distance between these two points in the
538 $e+1$ dimension, $D_{\tau,e+1}(t) = \|X_{\tau,e+1}(t_{nn}) - X_{\tau,e+1}(t)\|_2$, is larger than their distance in
539 the e dimension, $D_{\tau,e}(t) = \|X_{\tau,e}(t_{nn}) - X_{\tau,e}(t)\|_2$, these two points are deemed to be
540 false nearest neighbors; specifically, we used a threshold R for the ratio between two
541 distances $D_{\tau,e+1}(t)/D_{\tau,e}(t)$ to determine false nearest neighbors. The first embed-
542 ding dimension e that does not have any false nearest neighbors corresponds to the

543 embedding dimension M for a given pathogen-country pair. For the main analysis,
 544 we used $R = 10$, which was chosen from a sensitivity analysis against simulated data
 545 (Supplementary Text). Once we determined the embedding lag τ and dimension M ,
 546 we apply the embedding to the entire time series and calculate the nearest neighbor
 547 distance against the attractor $A_{\tau,M}$ to obtain a time series of distance from the
 548 attractor $D_{\tau,M}(t)$.

549 From a time series of distances from the attractor, we estimated pathogen resilience
 550 by fitting a linear regression to an appropriate window. To automatically
 551 select fitting windows, we began by smoothing the distance time series using locally
 552 estimated scatterplot smoothing (LOESS) to obtain $\hat{D}_{\tau,M}(t)$, where the smoothing
 553 is performed on a log scale and exponentiated afterwards. This smoothing allowed
 554 us to find appropriate threshold values for selecting fitting windows that are insensitive
 555 to errors in our estimates of distance from the attractor. Then, we determined
 556 threshold values (T_{start} and T_{end}) for the smoothed distances and choose the fitting
 557 window based on when $\hat{D}_{\tau,M}(t)$ crosses these threshold values for the first time.
 558 These thresholds were determined by first calculating the maximum distance,

$$\max \hat{D} = \max \hat{D}_{\tau,M}(t), \quad (3)$$

559 and the mean pre-pandemic distance,

$$\hat{D}_{\text{mean}} = \frac{1}{N_{t < 2020}} \sum_{t < 2020} \hat{D}_{\tau,M}(t), \quad (4)$$

560 as a reference, and then dividing their ratios into K equal bins,

$$T_{\text{start}} = \hat{D}_{\text{mean}} \times \left(\frac{\max \hat{D}}{\hat{D}_{\text{mean}}} \right)^{(K-a)/K}, \quad (5)$$

$$T_{\text{end}} = \hat{D}_{\text{mean}} \times \left(\frac{\max \hat{D}}{\hat{D}_{\text{mean}}} \right)^{a/K}, \quad (6)$$

561 where a represents the truncation threshold. This allows us to discard the initial
 562 period during which the distance increases (from the introduction of intervention
 563 measures) and the final period during which the distance plateaus (as the system
 564 reaches an attractor). The fitting window is determined based on when the smoothed
 565 distance $\hat{D}_{\tau,M}(t)$ crosses these threshold values for the first time; then, we fit a
 566 linear regression to logged (unsmoothed) distances $\log D_{\tau,M}(t)$ using that window.
 567 Alongside the threshold R for the false nearest neighbors approach, we tested optimal
 568 choices for K and a values using simulations (Supplementary Text). We used $K = 19$
 569 and $a = 2$ throughout the paper based on the simulation results.

570 Mathematical modeling

571 Throughout the paper, we use a series of mathematical models to illustrate the
 572 concept of pathogen resilience and to understand the determinants of pathogen re-

573 silience. In general, the intrinsic resilience of a given system is given by the largest
 574 real part of the eigenvalues of the linearized system at endemic equilibrium. Here, we
 575 focus on the SIRS model with demography (birth and death) and present the details
 576 of other models in Supplementary Text. The SIRS (Susceptible-Infected-Recovered-
 577 Susceptible) model is the simplest model that allows for waning of immunity, where
 578 recovered (immune) individuals are assumed to become fully susceptible after an
 579 average of $1/\delta$ time period. The dynamics of the SIRS model is described by the
 580 following set of differential equations:

$$\frac{dS}{dt} = \mu - \beta(t)SI - \mu S + \delta R \quad (7)$$

$$\frac{dI}{dt} = \beta(t)SI - (\gamma + \mu)I \quad (8)$$

$$\frac{dR}{dt} = \gamma I - (\delta + \mu)R \quad (9)$$

581 where μ represents the birth and death rates, $\beta(t)$ represents the time-varying trans-
 582 mission rate, and γ represents the recovery rate. The basic reproduction number
 583 $\mathcal{R}_0(t) = \beta(t)/(\gamma + \mu)$ is defined as the average number of secondary infections that
 584 a single infected individual would cause in a fully susceptible population at time t
 585 and measures the intrinsic transmissibility of a pathogen.

586 When we introduced the idea of pathogen resilience (Figure 2), we imposed sinu-
 587 soidal changes to the transmission rate to account for seasonal transmission,

$$\beta(t) = b_1(1 + \theta \cos(2\pi(t - \phi)))\alpha(t), \quad (10)$$

588 where b_1 represents the baseline transmission rate, θ represents the seasonal ampli-
 589 tude, and ϕ represents the seasonal offset term. Here, we also introduced an extra
 590 multiplicative term $\alpha(t)$ to account for the impact of pandemic perturbations, where
 591 $\alpha(t) < 1$ indicates transmission reduction. Figure 2A and 2B were generated assum-
 592 ing $b_1 = 3 \times (365/7 + 1/50)/\text{years}$, $\theta = 0.2$, $\phi = 0$, $\mu = 1/50/\text{years}$, $\gamma = 365/7/\text{years}$,
 593 and $\delta = 1/2/\text{years}$. Specifically, $b_1 = 3 \times (365/7 + 1/50)/\text{years}$ implies $\mathcal{R}_0 = 3$, where
 594 $(365/7 + 1/50)/\text{years}$ represent the rate of recovery. In Figure 2A, we imposed a 50%
 595 transmission reduction for 6 months from 2020:

$$\alpha(t) = \begin{cases} 0.5 & 2020 \leq t < 2020.5 \\ 1 & \text{otherwise} \end{cases} \quad (11)$$

596 In Figure 2B, we imposed a 50% transmission reduction for 6 months from 2020 and
 597 a permanent 10% reduction onward:

$$\alpha(t) = \begin{cases} 1 & t < 2020 \\ 0.5 & 2020 \leq t < 2020.5 \\ 0.9 & 2020.5 \leq t \end{cases} \quad (12)$$

598 In both scenarios, we simulated the SIRS model from the same initial conditions
 599 ($S(0) = 1/\mathcal{R}_0$, $I(0) = 1 \times 10^{-6}$, and $R(0) = 1 - S(0) - I(0)$) from 1900 until 2030.
 600 Throughout the paper, all deterministic models were solved using the `lsoda` solver
 601 from the `deSolve` package [46] in R [47].

602 To measure the empirical resilience of the SIRS model (Figure 2C and 2F), we
 603 computed the normalized distance between post-intervention susceptible and logged
 604 infected proportions and their corresponding unperturbed values at the same time:

$$\sqrt{\left(\frac{S(t) - S_{\text{unperturbed}}(t)}{\sigma_S}\right)^2 + \left(\frac{\log I(t) - \log I_{\text{unperturbed}}(t)}{\sigma_{\log I}}\right)^2}, \quad (13)$$

605 where σ_S and $\sigma_{\log I}$ represent the standard deviation in the unperturbed susceptible
 606 and logged infected proportions. The unperturbed values were obtained by simulating
 607 the same SIRS model without pandemic perturbations ($\alpha = 1$). We normalized
 608 the differences in susceptible and logged infected proportions to allow both quantities
 609 to equally contribute to the changes in distance from the attractor. We used logged
 610 prevalence, instead of absolute prevalence, in order to capture epidemic dynamics
 611 in deep troughs during the intervention period. In Supplementary Materials, we
 612 also compared how the degree of seasonal transmission affects empirical resilience
 613 by varying θ from 0 to 0.4; when we assumed no seasonality ($\theta = 0$), we did not
 614 normalize the distance because the standard deviation of pre-intervention dynamics
 615 are zero.

616 We used the SIRS model to understand how underlying epidemiological parameters
 617 affect pathogen resilience and determine the relationship to underlying susceptible host dynamics. For the simple SIRS model without seasonal transmission
 618 ($\theta = 0$), the intrinsic resilience equals

$$-\frac{\text{Re}(\lambda)}{2} = \frac{\delta + \beta I^* + \mu}{2}. \quad (14)$$

620 Here, I^* represents the prevalence at endemic equilibrium:

$$I^* = \frac{(\delta + \mu)(\beta - (\gamma + \mu))}{\beta(\delta + \gamma + \mu)}. \quad (15)$$

621 The susceptible replenishment rate is given by

$$S_{\text{replenish}} = \frac{\mu + \delta R}{S^*}, \quad (16)$$

622 where $S^* = 1/\mathcal{R}_0$ represents the equilibrium proportion of susceptible individuals.
 623 We varied the basic reproduction number \mathcal{R}_0 between 1.1 to 6 and the average
 624 duration of immunity $1/\delta$ between 2 to 4 years, and computed these two quantities.
 625 In doing so, we fixed all other parameters: $\mu = 1/80/\text{years}$ and $\gamma = 365/7/\text{years}$.
 626 When infection provides a life-long immunity ($\delta = 0$), the intrinsic resilience is
 627 inversely proportional to the susceptible replenishment rate:

$$-\frac{\text{Re}(\lambda)}{2} = \frac{\mu}{2S^*} = \frac{S_{\text{replenish}}}{2}. \quad (17)$$

628 Finally, we used a seasonally unforced stochastic SIRS model without demog-
629 raphy to understand how pathogen resilience affects sensitivity of the system to
630 demographic stochasticity (see Supplementary Text for the details of the stochas-
631 tic SIRS model). By varying the basic reproduction number \mathcal{R}_0 between 2 to 20
632 and the average duration of immunity $1/\delta$ between 1 to 40 years, we ran the SIRS
633 model for 100 years and computed the epidemic amplitude, which we defined as
634 $(\max I - \min I)/(2\bar{I})$. Each simulation began from the equilibrium, and we trun-
635 cated the initial 25 years before computing the epidemic amplitude. In doing so,
636 we assumed $\gamma = 365/7/\text{years}$ and fixed the population size to 1 billion to prevent
637 any fadeouts. We also considered a seasonally forced stochastic SIRS model without
638 demography, assuming an amplitude of seasonal forcing of 0.04; in this case, we com-
639 puted the relative epidemic amplitude by comparing the deterministic and stochastic
640 trajectories (Supplementary Materials).

641 Acknowledgement

642 We thank Centers for Disease Control and Prevention, National Respiratory and
643 Enteric Virus Surveillance System (NREVSS) for providing time series data for res-
644 piratory infection cases in the US.

645 Data availability

646 All data and code are stored in a publicly available GitHub repository (<https://github.com/cobeylab/return-time>).

648 Funding

649 S.W.P. is a Peter and Carmen Lucia Buck Foundation Awardee of the Life Sciences
650 Research Foundation. B.F.N. acknowledges financial support from the Carlsberg
651 Foundation (grant no. CF23-0173). B.T.G is supported by Princeton Catalysis Ini-
652 tiative and Princeton Precision Health. S.C. is supported by Federal funds from the
653 National Institute of Allergy and Infectious Diseases, National Institutes of Health,
654 Department of Health and Human Services under CEIRR contract 75N93021C00015.
655 The content is solely the responsibility of the authors and does not necessarily repre-
656 sent the official views of the NIAID or the National Institutes of Health. This project
657 has been funded in whole or in part with Federal funds from the National Cancer In-
658 stitute, National Institutes of Health, under Prime Contract No. 75N91019D00024,
659 Task Order No. 75N91023F00016 (B.F.N., E.H., and B.T.G). The content of this
660 publication does not necessarily reflect the views or policies of the Department of
661 Health and Human Services, nor does mention of trade names, commercial products
662 or organizations imply endorsement by the U.S. Government.

663 **Supplementary Text**

664 **Resilience of a stage-structured system.**

665 In Figure 2G–I, we used a more realistic, stage-structured model to illustrate how
 666 transient phenomena can cause the system to slow down. Specifically, we used the
 667 stage-structured RSV model proposed by [26], which assumes that subsequent rein-
 668 fections cause an individual to become less susceptible and transmissible than previ-
 669 ous infections. In contrast to a standard SIRS model, this model does not include a
 670 recovered compartment, which allow for temporary protection against new infections,
 671 and assumes that recovered individuals are immediately susceptible to new infections.
 672 The model dynamics can be described as follows:

$$\frac{dM}{dt} = \mu - (\omega + \mu)M \quad (S1)$$

$$\frac{dS_0}{dt} = \omega M - (\lambda(t) + \mu)S_0 \quad (S2)$$

$$\frac{dI_1}{dt} = \lambda(t)S_0 - (\gamma_1 + \mu)I_1 \quad (S3)$$

$$\frac{dS_1}{dt} = \gamma_1 I_1 - (\sigma_1 \lambda(t) + \mu)S_1 \quad (S4)$$

$$\frac{dI_2}{dt} = \sigma_1 \lambda(t)S_1 - (\gamma_2 + \mu)I_2 \quad (S5)$$

$$\frac{dS_2}{dt} = \gamma_2 I_2 - (\sigma_2 \lambda(t) + \mu)S_2 \quad (S6)$$

$$\frac{dI_3}{dt} = \sigma_2 \lambda(t)S_2 - (\gamma_3 + \mu)I_3 \quad (S7)$$

$$\frac{dS_3}{dt} = \gamma_3 I_3 - (\sigma_3 \lambda(t) + \mu)S_3 + \gamma_4 I_4 \quad (S8)$$

$$\frac{dI_4}{dt} = \sigma_3 \lambda(t)S_3 - (\gamma_4 + \mu)I_4 \quad (S9)$$

673 where M represents the proportion of individuals who are maternally immune; S_i
 674 represents the proportion of individuals who are susceptible after i prior infections; I_i
 675 represents the proportion of individuals who are currently (re)-infected with their i -th
 676 infection; μ represents the birth and death rates; $1/\omega$ represents the mean duration
 677 of maternal immunity; $1/\gamma_i$ represents the mean duration of infection; $\lambda(t)$ represents
 678 the force of infection; and σ_i represents the reduction in susceptibility for the i -th
 679 reinfection. The force of infection is modeled using a sinusoidal function:

$$\beta(t) = b_1(1 + \theta \cos(2\pi(t - \phi)))\alpha(t) \quad (S10)$$

$$\lambda(t) = \beta(I_1 + \rho_1 I_2 + \rho_2(I_3 + I_4)), \quad (S11)$$

680 where b_1 represents the baseline transmission rate; θ represents the seasonal ampli-
 681 tude; ϕ represents the seasonal offset term; $\alpha(t)$ represents the intervention effect;

and ρ_i represents the impact of immunity on transmission reduction. We used the following parameters to simulate the impact of interventions on epidemic dynamics [26]: $b_1 = 9 \times (365/10 + 1/80)/\text{years}$, $\theta = 0.2$, $\phi = -0.1$, $\omega = 365/112/\text{years}$, $\gamma_1 = 365/10/\text{years}$, $\gamma_2 = 365/7/\text{years}$, $\gamma_3 = 365/5/\text{years}$, $\sigma_1 = 0.76$, $\sigma_2 = 0.6$, $\sigma_3 = 0.4$, $\rho_1 = 0.75$, $\rho_2 = 0.51$, and $\mu = 1/80/\text{years}$. We assumed a 50% transmission reduction for 6 months from 2020:

$$\alpha(t) = \begin{cases} 0.5 & 2020 \leq t < 2020.5 \\ 1 & \text{otherwise} \end{cases} \quad (\text{S12})$$

The model was simulated from 1900 to 2030 using the following initial conditions: $M = 0$, $S_0 = 1/\mathcal{R}_0 - I_1$, $I_1 = 1 \times 10^{-6}$, $S_1 = 1 - 1/\mathcal{R}_0$, $I_2 = 0$, $S_2 = 0$, $I_3 = 0$, $S_3 = 0$, and $I_4 = 0$. For the phase plane analysis (Figure 2H) and distance analysis (Figure 2I), we relied on the average susceptibility,

$$\bar{S} = S_0 + \sigma_1 S_1 + \sigma_2 S_2 + \sigma_3 S_3, \quad (\text{S13})$$

and total prevalence,

$$I_{\text{total}} = I_1 + I_2 + I_3 + I_4. \quad (\text{S14})$$

These quantities were used to compute the normalized distance from the attractor, as described in the main text.

We note that this system, without seasonally forced transmission rates, has 9 eigenvalues: -73.01, -53.11, -38.90, -3.27, $-0.82+2.57i$, $-0.82-2.57i$, -1.61, -1.18, and -0.01 (in the unit of 1/years). While the eigenvalue -0.01 has the largest real part, the magnitude is too close to 0 for the impact of this eigenvalue to be reflected in our resilience estimates. Instead, we chose real parts of the eigenvalues $-0.82 \pm 2.57i$ as our intrinsic resilience for this system and plotted them in Figure 2I; as we can see in this figure, this value captures the return rate of the system to the attractor.

Resilience of a multistrain system.

We used a simple two-strain model to show that a multistrain host-pathogen system that is coupled through cross immunity can be described by a single resilience value. The model dynamics can be described as follows [34]:

$$\frac{dS}{dt} = \mu - \mu S - (\lambda_1 + \lambda_2)S + \delta_1 R_1 + \delta_2 R_2 \quad (\text{S15})$$

$$\frac{dI_1}{dt} = \lambda_1 S - (\gamma_1 + \mu)I_1 \quad (\text{S16})$$

$$\frac{dI_2}{dt} = \lambda_2 S - (\gamma_2 + \mu)I_2 \quad (\text{S17})$$

$$\frac{dR_1}{dt} = \gamma_1 I_1 - \lambda_2 \epsilon_{21} R_1 - \delta_1 R_1 + \delta_2 R - \mu R_1 \quad (\text{S18})$$

$$\frac{dR_2}{dt} = \gamma_2 I_2 - \lambda_1 \epsilon_{12} R_2 - \delta_2 R_2 + \delta_1 R - \mu R_2 \quad (\text{S19})$$

$$\frac{dJ_1}{dt} = \lambda_1 \epsilon_{12} R_2 - (\gamma_1 + \mu) J_1 \quad (S20)$$

$$\frac{dJ_2}{dt} = \lambda_2 \epsilon_{21} R_1 - (\gamma_2 + \mu) J_2 \quad (S21)$$

$$\frac{dR}{dt} = \gamma_1 J_1 + \gamma_2 J_2 - \delta_1 R - \delta_2 R - \mu R \quad (S22)$$

where S represents the proportion of individuals who are fully susceptible to infections by both strains; I_1 represents the proportion of individuals who are infected with strain 1 without prior immunity; I_2 represents the proportion of individuals who are infected with strain 2 without prior immunity; R_1 represents the proportion of individuals who are fully immune against strain 1 and partially susceptible to reinfection by strain 2; R_2 represents the proportion of individuals who are fully immune against strain 2 and partially susceptible to reinfection by strain 1; J_1 represents the proportion of individuals who are infected with strain 1 with prior immunity against strain 2; J_2 represents the proportion of individuals who are infected with strain 2 with prior immunity against strain 1; R represents the proportion of individuals who are immune to infections from both strains; μ represents the birth/death rate; λ_1 and λ_2 represent the force of infection from strains 1 and 2, respectively; δ_1 and δ_2 represent the waning immunity rate; γ_1 and γ_2 represent the recovery rate; ϵ_{21} and ϵ_{12} represent the susceptibility to reinfection with strains 2 and 1, respectively, given prior immunity from infection with strains 1 and 2, respectively. The force of infection is modeled as follows:

$$\beta_1 = b_1(1 + \theta_1 \sin(2\pi(t - \phi_1)))\alpha(t) \quad (S23)$$

$$\beta_2 = b_2(1 + \theta_2 \sin(2\pi(t - \phi_2)))\alpha(t) \quad (S24)$$

$$\lambda_1 = \beta_1(I_1 + J_1) \quad (S25)$$

$$\lambda_2 = \beta_2(I_2 + J_2) \quad (S26)$$

In Supplementary Figures S2–S4, we assumed the following parameters: $b_1 = 2 \times 52/\text{years}$, $b_2 = 4 \times 52/\text{years}$, $\phi_1 = \phi_2 = 0$, $\epsilon_{12} = 0.9$, $\epsilon_{21} = 0.5$, $\gamma_1 = \gamma_2 = 52/\text{years}$, $\delta_1 = \delta_2 = 1/\text{years}$, and $\mu = 1/70/\text{years}$. For all simulations, we assumed a 50% transmission reduction for 6 months from 2020:

$$\alpha(t) = \begin{cases} 0.5 & 2020 \leq t < 2020.5 \\ 1 & \text{otherwise} \end{cases} \quad (S27)$$

The seasonal amplitude θ is varied from 0 to 0.4. All simulations were run from 1900 to 2030 with following initial conditions: $S(0) = 1 - 2 \times 10^{-6}$, $I_1(0) = 1 \times 10^{-6}$, $I_2(0) = 1 \times 10^{-6}$, $R_1(0) = 0$, $R_2(0) = 0$, $J_1(0) = 0$, $J_2(0) = 0$, and $R(0) = 0$.

We considered three scenarios for measuring pathogen resilience: (1) we only have information about strain 1, (2) we only have information about strain 2, and (3) we are unable to distinguish between strains. In the first two scenarios (see panels A–C for strain 1 and panels D–F for strain 2), we considered the dynamics of average

⁷³³ susceptibility for each strain and total prevalence:

$$\bar{S}_1 = S + \epsilon_{12}R_2 \quad (\text{S28})$$

$$\hat{I}_1 = I_1 + J_1 \quad (\text{S29})$$

$$\bar{S}_2 = S + \epsilon_{21}R_1 \quad (\text{S30})$$

$$\hat{I}_2 = I_2 + J_2 \quad (\text{S31})$$

⁷³⁴ In the third scenario (panels G–I), we considered the dynamics of total susceptible
⁷³⁵ and infected populations:

$$\hat{S} = S + R_2 + R_1 \quad (\text{S32})$$

$$\hat{I} = I_1 + J_1 + I_2 + J_2 \quad (\text{S33})$$

⁷³⁶ These quantities were used to compute the normalized distance from the attractor,
⁷³⁷ as described in the main text.

⁷³⁸ Estimating intrinsic resilience using a mechanistic model

⁷³⁹ We tested whether we can reliably estimate the intrinsic resilience of a system by fit-
⁷⁴⁰ ting a mechanistic model. Specifically, we simulated case time series from stochastic
⁷⁴¹ SIRS and two-strain models and fitted a simple, deterministic SIRS model using a
⁷⁴² Bayesian framework [4, 23, 48].

⁷⁴³ We simulated the models in discrete time with a daily time step ($\Delta t = 1$),
⁷⁴⁴ incorporating demographic stochasticity:

$$\beta(t) = \mathcal{R}_0 \left(1 + \theta \cos \left(\frac{2\pi t}{364} \right) \right) \alpha(t)(1 - \exp(-\gamma)) \quad (\text{S34})$$

$$\text{FOI}(t) = \beta(t)I(t - \Delta t)/N \quad (\text{S35})$$

$$B(t) \sim \text{Poisson}(\mu N) \quad (\text{S36})$$

$$\Delta S(t) \sim \text{Binom}(S(t - \Delta t), 1 - \exp(-(\text{FOI}(t) + \mu)\Delta t)) \quad (\text{S37})$$

$$N_{SI}(t) \sim \text{Binom}\left(\Delta S(t), \frac{\text{FOI}(t)}{\text{FOI}(t) + \mu}\right) \quad (\text{S38})$$

$$\Delta I(t) \sim \text{Binom}(I(t - \Delta t), 1 - \exp(-(\gamma + \mu)\Delta t)) \quad (\text{S39})$$

$$N_{IR}(t) \sim \text{Binom}\left(\Delta I(t), \frac{\gamma}{\gamma + \mu}\right) \quad (\text{S40})$$

$$\Delta R(t) \sim \text{Binom}(R(t - \Delta t), 1 - \exp(-(\delta + \mu)\Delta t)) \quad (\text{S41})$$

$$N_{RS}(t) \sim \text{Binom}\left(\Delta R(t), \frac{\delta}{\delta + \mu}\right) \quad (\text{S42})$$

$$S(t) = S(t - \Delta t) + N_{RS}(t) + B(t) - \Delta S(t) \quad (\text{S43})$$

$$I(t) = I(t - \Delta t) + N_{SI}(t) - \Delta I(t) \quad (\text{S44})$$

$$R(t) = R(t - \Delta t) + N_{IR}(t) - \Delta R(t) \quad (\text{S45})$$

where FOI represents the force of infection; N_{ij} represents the number of individuals moving from compartment i to j on a given day; and $B(t)$ represents the number of new births. All other parameters definitions can be found in the description of the deterministic version of the model. We simulated the model on a daily scale—assuming 364 days in a year so that it can be evenly grouped into 52 weeks—with the following parameters: $\mathcal{R}_0 = 3$, $\theta = 0.1$, $\gamma = 1/7/\text{days}$, $\delta = 1/(364 \times 2)/\text{days}$, $\mu = 1/(364 \times 50)/\text{days}$, and $N = 1 \times 10^8$. The model was simulated from 1900 to 2030 assuming $S(0) = N/3$, $I(0) = 100$, and $R(0) = N - S(0) - I(0)$. The observed incidence from the model was then simulated as follows:

$$C(t) = \text{Beta-Binom}(N_{SI}(t), \rho, k), \quad (\text{S46})$$

where ρ represents the reporting probability and k represents the overdispersion parameter of beta-binomial distribution. Here, we used the beta-binomial distribution to account for overdispersion in reporting. We assumed $\rho = 0.002$ (i.e., 0.2% probability) and $k = 1000$.

We used an analogous approach for the two-strain model:

$$\beta_1(t) = b_1 \left(1 + \theta_1 \cos \left(\frac{2\pi(t - \phi_1)}{364} \right) \right) \alpha(t) \quad (\text{S47})$$

$$\beta_2(t) = b_2 \left(1 + \theta_2 \cos \left(\frac{2\pi(t - \phi_2)}{364} \right) \right) \alpha(t) \quad (\text{S48})$$

$$\text{FOI}_1(t) = \beta_1(t)(I_1(t - \Delta t) + J_1(t - \Delta t))/N \quad (\text{S49})$$

$$\text{FOI}_2(t) = \beta_2(t)(I_2(t - \Delta t) + J_2(t - \Delta t))/N \quad (\text{S50})$$

$$B(t) \sim \text{Poisson}(\mu N) \quad (\text{S51})$$

$$\Delta S(t) \sim \text{Binom}(S(t - \Delta t), 1 - \exp(-(\text{FOI}_1(t) + \text{FOI}_2(t) + \mu)\Delta t)) \quad (\text{S52})$$

$$N_{SI_1}(t) \sim \text{Binom}\left(\Delta S(t), \frac{\text{FOI}_1(t)}{\text{FOI}_1(t) + \text{FOI}_2(t) + \mu}\right) \quad (\text{S53})$$

$$N_{SI_2}(t) \sim \text{Binom}\left(\Delta S(t), \frac{\text{FOI}_2(t)}{\text{FOI}_1(t) + \text{FOI}_2(t) + \mu}\right) \quad (\text{S54})$$

$$\Delta I_1(t) \sim \text{Binom}(I_1(t - \Delta t), 1 - \exp(-(\gamma_1 + \mu)\Delta t)) \quad (\text{S55})$$

$$N_{I_1 R_1}(t) \sim \text{Binom}\left(\Delta I_1(t), \frac{\gamma_1}{\gamma_1 + \mu}\right) \quad (\text{S56})$$

$$\Delta I_2(t) \sim \text{Binom}(I_2(t - \Delta t), 1 - \exp(-(\gamma_2 + \mu)\Delta t)) \quad (\text{S57})$$

$$N_{I_2 R_2}(t) \sim \text{Binom}\left(\Delta I_2(t), \frac{\gamma_2}{\gamma_2 + \mu}\right) \quad (\text{S58})$$

$$\Delta R_1(t) \sim \text{Binom}(R_1(t - \Delta t), 1 - \exp(-(\epsilon_{21}\text{FOI}_2(t) + \rho_1 + \mu)\Delta t)) \quad (\text{S59})$$

$$N_{R_1 S}(t) \sim \text{Binom}\left(\Delta R_1(t), \frac{\rho_1}{\epsilon_{21}\text{FOI}_2(t) + \rho_1 + \mu}\right) \quad (\text{S60})$$

$$N_{R_1 J_2}(t) \sim \text{Binom}\left(\Delta R_1(t), \frac{\epsilon_{21}\text{FOI}_2(t)}{\epsilon_{21}\text{FOI}_2(t) + \rho_1 + \mu}\right) \quad (\text{S61})$$

$$\Delta R_2(t) \sim \text{Binom}(R_2(t - \Delta t), 1 - \exp(-(\epsilon_{12}\text{FOI}_1(t) + \rho_2 + \mu)\Delta t)) \quad (\text{S62})$$

$$N_{R_2S}(t) \sim \text{Binom}\left(\Delta R_2(t), \frac{\rho_2}{\epsilon_{12}\text{FOI}_1(t) + \rho_2 + \mu}\right) \quad (\text{S63})$$

$$N_{R_2J_1}(t) \sim \text{Binom}\left(\Delta R_2(t), \frac{\epsilon_{12}\text{FOI}_1(t)}{\epsilon_{12}\text{FOI}_1(t) + \rho_2 + \mu}\right) \quad (\text{S64})$$

$$\Delta J_1(t) \sim \text{Binom}(J_1(t - \Delta t), 1 - \exp(-(\gamma_1 + \mu)\Delta t)) \quad (\text{S65})$$

$$N_{J_1R}(t) \sim \text{Binom}\left(\Delta J_1(t), \frac{\gamma_1}{\gamma_1 + \mu}\right) \quad (\text{S66})$$

$$\Delta J_2(t) \sim \text{Binom}(J_2(t - \Delta t), 1 - \exp(-(\gamma_2 + \mu)\Delta t)) \quad (\text{S67})$$

$$N_{J_2R}(t) \sim \text{Binom}\left(\Delta J_2(t), \frac{\gamma_2}{\gamma_2 + \mu}\right) \quad (\text{S68})$$

$$\Delta R(t) \sim \text{Binom}(R(t - \Delta t), 1 - \exp(-(\rho_1 + \rho_2 + \mu)\Delta t)) \quad (\text{S69})$$

$$N_{RR_1}(t) \sim \text{Binom}\left(\Delta R(t), \frac{\rho_1}{\rho_1 + \rho_2 + \mu}\right) \quad (\text{S70})$$

$$N_{RR_2}(t) \sim \text{Binom}\left(\Delta R(t), \frac{\rho_2}{\rho_1 + \rho_2 + \mu}\right) \quad (\text{S71})$$

$$S(t) = S(t - \Delta t) - \Delta S(t) + B(t) + N_{R_1S}(t) + N_{R_2S}(t) \quad (\text{S72})$$

$$I_1(t) = I_1(t - \Delta t) - \Delta I_1(t) + N_{SI_1}(t) \quad (\text{S73})$$

$$I_2(t) = I_2(t - \Delta t) - \Delta I_2(t) + N_{SI_2}(t) \quad (\text{S74})$$

$$R_1(t) = R_1(t - \Delta t) - \Delta R_1(t) + N_{I_1R_1}(t) + N_{RR_1}(t) \quad (\text{S75})$$

$$R_2(t) = R_2(t - \Delta t) - \Delta R_2(t) + N_{I_2R_2}(t) + N_{RR_2}(t) \quad (\text{S76})$$

$$J_1(t) = J_1(t - \Delta t) - \Delta J_1(t) + N_{R_2J_1}(t) \quad (\text{S77})$$

$$J_2(t) = J_2(t - \Delta t) - \Delta J_2(t) + N_{R_1J_2}(t) \quad (\text{S78})$$

$$R(t) = R(t - \Delta t) - \Delta R(t) + N_{J_1R}(t) + N_{J_2R}(t) \quad (\text{S79})$$

We simulated the model on a daily scale with previously estimated parameters for the RSV-HMPV interaction [34]: $b_1 = 1.7/\text{weeks}$, $b_2 = 1.95/\text{weeks}$, $\theta_1 = 0.4$, $\theta_2 = 0.3$, $\phi_1 = 0.005 \times 7/364$, $\phi_2 = 4.99 \times 7/364$, $\epsilon_{12} = 0.92$, $\epsilon_{21} = 0.45$, $\gamma_1 = 1/10/\text{days}$, $\gamma_2 = 1/10/\text{days}$, $\rho_1 = 1/364/\text{days}$, $\rho_2 = 1/364/\text{days}$, $\mu = 1/(70 \times 364)/\text{days}$, and $N = 1 \times 10^8$. The model was simulated from 1900 to 2030 assuming $S(0) = N - 200$, $I_1(0) = 100$, $I_2(0) = 100$, $R_1(0) = 0$, $R_2(0) = 0$, $J_1(0) = 0$, $J_2(0) = 0$, and $R(0) = 0$. The observed incidence for each strain is then simulated as follows:

$$C_1(t) = \text{Beta-Binom}(N_{SI_1}(t) + N_{R_2J_1}, \rho, k), \quad (\text{S80})$$

$$C_2(t) = \text{Beta-Binom}(N_{SI_2}(t) + N_{R_1J_2}, \rho, k), \quad (\text{S81})$$

where ρ represents the reporting probability and k represents the overdispersion parameter of beta-binomial distribution. We assumed $\rho = 0.002$ (i.e., 0.2% probability) and $k = 500$. We also considered the total incidence: $C_{\text{total}}(t) = C_1(t) + C_2(t)$.

For both models, we considered a more realistically shaped pandemic perturbation $\alpha(t)$ to challenge our ability to estimate the intervention effects. Thus, we

⁷⁷¹ assumed a 40% transmission reduction for 3 months from March 2020, followed by a
⁷⁷² 10% transmission reduction for 6 months, 20% transmission reduction for 3 months,
⁷⁷³ and a final return to normal levels:

$$\alpha(t) = \begin{cases} 1 & t < 2020.25 \\ 0.6 & 2020.25 \leq t < 2020.5 \\ 0.9 & 2020.5 \leq t < 2021 \\ 0.8 & 2021 \leq t < 2021.25 \\ 1 & 2021.25 \leq t \end{cases}. \quad (\text{S82})$$

⁷⁷⁴ For all simulations, we truncated the time series from the beginning of 2014 to the
⁷⁷⁵ end of 2023 and aggregated them into weekly cases.

⁷⁷⁶ To infer intrinsic resilience from time series, we fitted a simple discrete time,
⁷⁷⁷ deterministic SIRS model in a Bayesian framework [4]:

$$\Delta t = 1 \text{ week} \quad (\text{S83})$$

$$\text{FOI}(t) = \beta(t)(I(t - \Delta t) + \omega)/N \quad (\text{S84})$$

$$\Delta S(t) = [1 - \exp(-(\text{FOI}(t) + \mu)\Delta t)] S(t - \Delta t) \quad (\text{S85})$$

$$N_{SI}(t) = \frac{\text{FOI}(t)\Delta S(t)}{\text{FOI}(t) + \mu} \quad (\text{S86})$$

$$\Delta I(t) = [1 - \exp(-(\gamma + \mu)\Delta t)] I(t - \Delta t) \quad (\text{S87})$$

$$N_{IR}(t) = \frac{\gamma \Delta I(t)}{\gamma + \mu} \quad (\text{S88})$$

$$\Delta R(t) = [1 - \exp(-(\nu + \mu)\Delta t)] R(t - \Delta t) \quad (\text{S89})$$

$$N_{RS}(t) = \frac{\nu \Delta R(t)}{\nu + \mu} \quad (\text{S90})$$

$$S(t) = S(t - \Delta t) + \mu S - \Delta S(t) + N_{RS}(t) \quad (\text{S91})$$

$$I(t) = I(t - \Delta t) - \Delta I(t) + N_{SI}(t) \quad (\text{S92})$$

$$R(t) = R(t - \Delta t) - \Delta R(t) + N_{IR}(t) \quad (\text{S93})$$

⁷⁷⁸ where we include an extra term ω to account for importation. Although actual
⁷⁷⁹ simulations did not include any importation, we had found that including this term
⁷⁸⁰ generally helped with model convergence in previous analyses [4]. The transmission
⁷⁸¹ rate was divided into a seasonal term $\beta_{\text{seas}}(t)$ (repeated every year) and intervention
⁷⁸² term $\alpha(t)$, which were estimated jointly:

$$\beta(t) = \beta_{\text{seas}}(t)\alpha(t), \quad (\text{S94})$$

⁷⁸³ where $\alpha < 1$ corresponds to reduction in transmission due to intervention effects. To
⁷⁸⁴ constrain the smoothness of $\beta_{\text{seas}}(t)$, we imposed cyclic, random-walk priors:

$$\beta_{\text{seas}}(t) \sim \text{Normal}(\beta_{\text{seas}}(t - 1), \sigma) \quad t = 2 \dots 52 \quad (\text{S95})$$

$$\beta_{\text{seas}}(1) \sim \text{Normal}(\beta_{\text{seas}}(52), \sigma) \quad (\text{S96})$$

$$\sigma \sim \text{Half-Normal}(0, 1) \quad (\text{S97})$$

785 We fixed $\alpha(t) = 1$ for all $t < 2020$ and estimate α assuming a normal prior:

$$\alpha \sim \text{Normal}(1, 0.25). \quad (\text{S98})$$

786 We assumed weakly informative priors on ω and ν :

$$\omega \sim \text{Half-Normal}(0, 200) \quad (\text{S99})$$

$$\nu \sim \text{Normal}(104, 26) \quad (\text{S100})$$

787 We assumed that the true birth/death rates, population sizes, and recovery rates
788 are known. We note, however, that assuming $\gamma = 1/\text{week}$ actually corresponds to
789 a mean simulated infectious period of 1.6 weeks due to a time discretization, which
790 is much longer than the true value; this approximation allows us to test whether we
791 can still robustly estimate the intrinsic resilience given parameter mis-specification.
792 Initial conditions were estimated with following priors:

$$S(0) = Ns(0) \quad (\text{S101})$$

$$I(0) = Ni(0) \quad (\text{S102})$$

$$s(0) \sim \text{Uniform}(0, 1) \quad (\text{S103})$$

$$i(0) \sim \text{Half-Normal}(0, 0.001) \quad (\text{S104})$$

793 Finally, the observation model was specified as follows:

$$\text{Cases}(t) \sim \text{Negative-Binomial}(\rho N_{SI}(t), \phi) \quad (\text{S105})$$

$$\rho \sim \text{Half-Normal}(0, 0.02) \quad (\text{S106})$$

$$\phi \sim \text{Half-Normal}(0, 10) \quad (\text{S107})$$

794 where ρ represents the reporting probability and ϕ represents the negative binomial
795 overdispersion parameter.

796 The model was fitted to four separate time series: (1) incidence time series from
797 the SIRS model, (2) incidence time series for strain 1 from the two-strain model,
798 (3) incidence time series for strain 2 from the two-strain model, and (4) combined
799 incidence time series for strains 1 and 2 from the two-strain model. The model
800 was fitted using rstan [49, 50] with 4 chains, each consisting of 2000 iterations.
801 The resulting posterior distribution was used to calculate the intrinsic resilience of
802 the seasonally unforced SIRS model with the same parameters; eigenvalues of the
803 discrete-time SIR model were computed by numerically finding the equilibrium and
804 calculating the Jacobian matrix.

805 **Validations for window-selection criteria**

806 We used stochastic SIRS simulations to identify optimal parameters for the window-
 807 selection criteria that we used for the linear regression for estimating empirical re-
 808 silience. For each simulation, we began by generating a random perturbation $\alpha(t)$
 809 from a random set of parameters. First, we drew the duration of perturbation τ_{npi}
 810 from a uniform distribution between 1 and 2 years. Then, we drew independent
 811 normal variables z_i of length $[364\tau_{\text{npi}}]$ with a standard deviation of 0.02 and took a
 812 reverse cumulative sum to obtain a realistic shape for the perturbation:

$$x_n = 1 + \sum_{i=n}^{[364\tau_{\text{npi}}]} z_i, \quad n = 1, \dots, [364\tau_{\text{npi}}]. \quad (\text{S108})$$

813 In contrast to simple perturbations that assume a constant reduction in transmis-
 814 sion, this approach allows us to model transmission reduction that varies over time
 815 smoothly. We repeated this random generation process until less than 10% of x_n
 816 exceeds 1—this was done to ensure the perturbation term $\alpha(t)$ stays below 1 (and
 817 therefore reduce transmission) for the most part. Then, we set any values that are
 818 above 1 or below 0 to 1 and 0, respectively. Then, we randomly drew the minimum
 819 transmission during perturbation α_{\min} from a uniform distribution between 0.5 and
 820 0.7 and scale x_n to have a minimum of α_{\min} :

$$x_{\text{scale},n} = \alpha_{\min} + (1 - \alpha_{\min}) \times \frac{x_n - \min x_n}{1 - \min x_n}. \quad (\text{S109})$$

821 This allowed us to simulate a realistically shaped perturbation:

$$\alpha(t) = \begin{cases} 1 & t < 2020 \\ x_{\text{scale},364(t-2020)} & 2020 \leq t < 2020 + \tau_{\text{npi}} \\ 1 & \tau_{\text{npi}} \leq t \end{cases}. \quad (\text{S110})$$

822 Given this perturbation function, we draw \mathcal{R}_0 from a uniform distribution between
 823 1.5 and 4 and the mean duration of immunity $1/\delta$ from a uniform distribution be-
 824 tween 1 and 4. Then, we simulate the stochastic SIRS model from $S(0) = 10^8/\mathcal{R}_0$
 825 and $I(0) = 100$ from 1990 to 2025 and truncate the time series to 2014–2025; if the
 826 epidemic becomes extinct before the end of simulation, we discard that simulation
 827 and start over from the perturbation generation step.

828 For each epidemic simulation, we computed the empirical resilience by varying
 829 the threshold R for the nearest neighbor approach from 4 to 14 with increments of
 830 2, the number of divisions K for the window selection between 8 and 25, and the
 831 truncation threshold a for the window selection between 1 to 3; this was done for all
 832 possible combinations of R , K , and a . We also compared this with the naive approach
 833 that uses the entire distance-from-attractor time series, starting from the maximum
 834 distance to the end of the time series. We repeated this procedure 500 times and
 835 quantified the correlation between empirical and intrinsic resilience estimates across
 836 two approaches.

Supplementary Figures

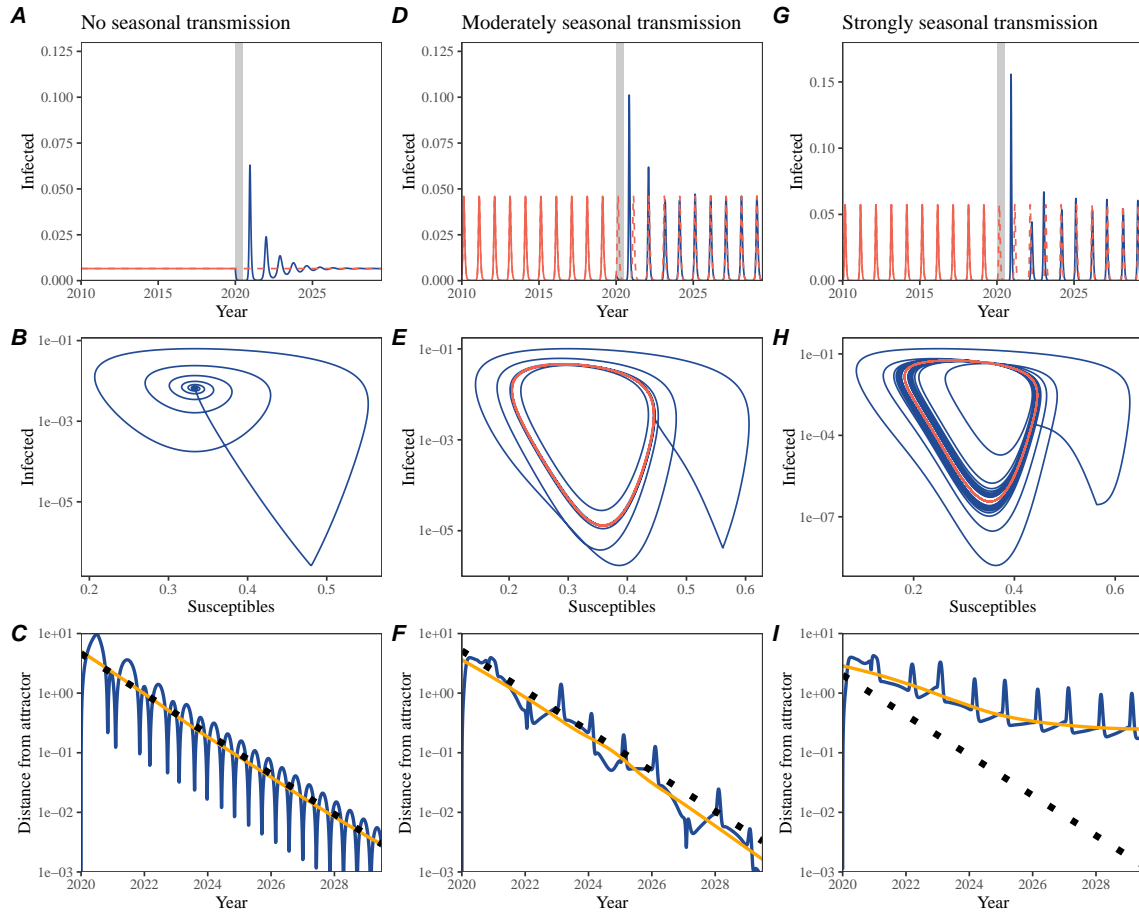


Figure S1: Impact of seasonal transmission on pathogen resilience. (A, D, G) Simulated epidemic trajectories using the SIRS model without seasonal forcing (A), with seasonal forcing of amplitude of 0.2 (D), and with seasonal forcing of amplitude of 0.4 (G). Red and blue solid lines represent epidemic dynamics before and after interventions are introduced, respectively. Red dashed lines represent counterfactual epidemic dynamics in the absence of interventions. Gray regions indicate the duration of interventions. (B, E, H) Phase plane representation of the time series in panels A, D, and G alongside the corresponding susceptible host dynamics. Red and blue solid lines represent epidemic trajectories on an SI phase plane before and after interventions are introduced, respectively. (C, F, I) Changes in logged distance from the attractor over time. Blue lines represent the logged distance from the attractor. Orange lines represent the locally estimated scatterplot smoothing (LOESS) fits to the logged distance from the attractor. Dotted lines show the intrinsic resilience of the seasonally unforced system.

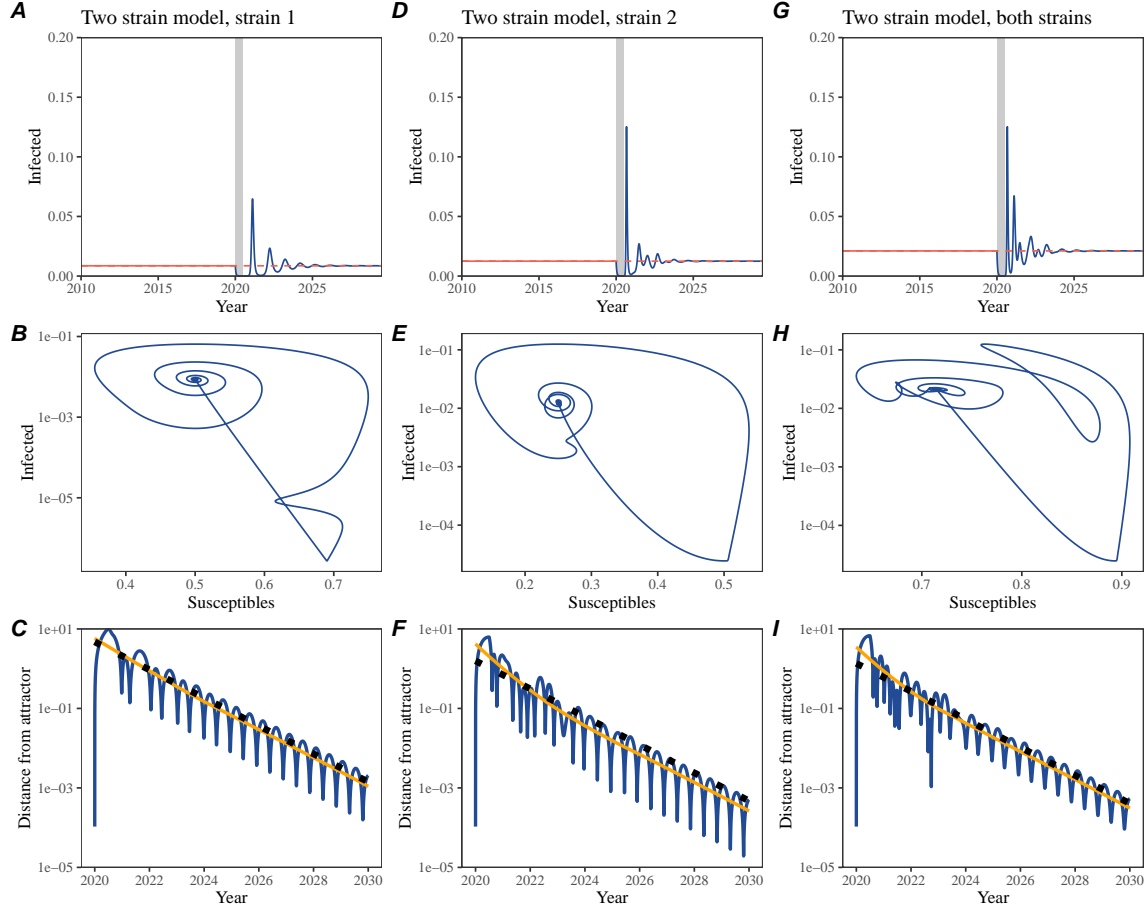


Figure S2: A simple method to measure pathogen resilience following pandemic perturbations for a two-strain competition system without seasonal forcing. (A, D, G) Simulated epidemic trajectories using a two-strain system without seasonal forcing. In this model, two strains compete through cross immunity. Red and blue solid lines represent epidemic dynamics before and after interventions are introduced, respectively. Red dashed lines represent counterfactual epidemic dynamics in the absence of interventions. Gray regions indicate the duration of interventions. (B, E, H) Phase plane representation of the time series in panels A, D, and G alongside the corresponding susceptible host dynamics. Blue solid lines represent epidemic trajectories on an SI phase plane before and after interventions. (C, F, I) Changes in logged distance from the attractor over time. Blue lines represent the logged distance from the attractor. Orange lines represent the locally estimated scatterplot smoothing (LOESS) fits to the logged distance from the attractor. Dotted lines show the intrinsic resilience of the seasonally unforced system.

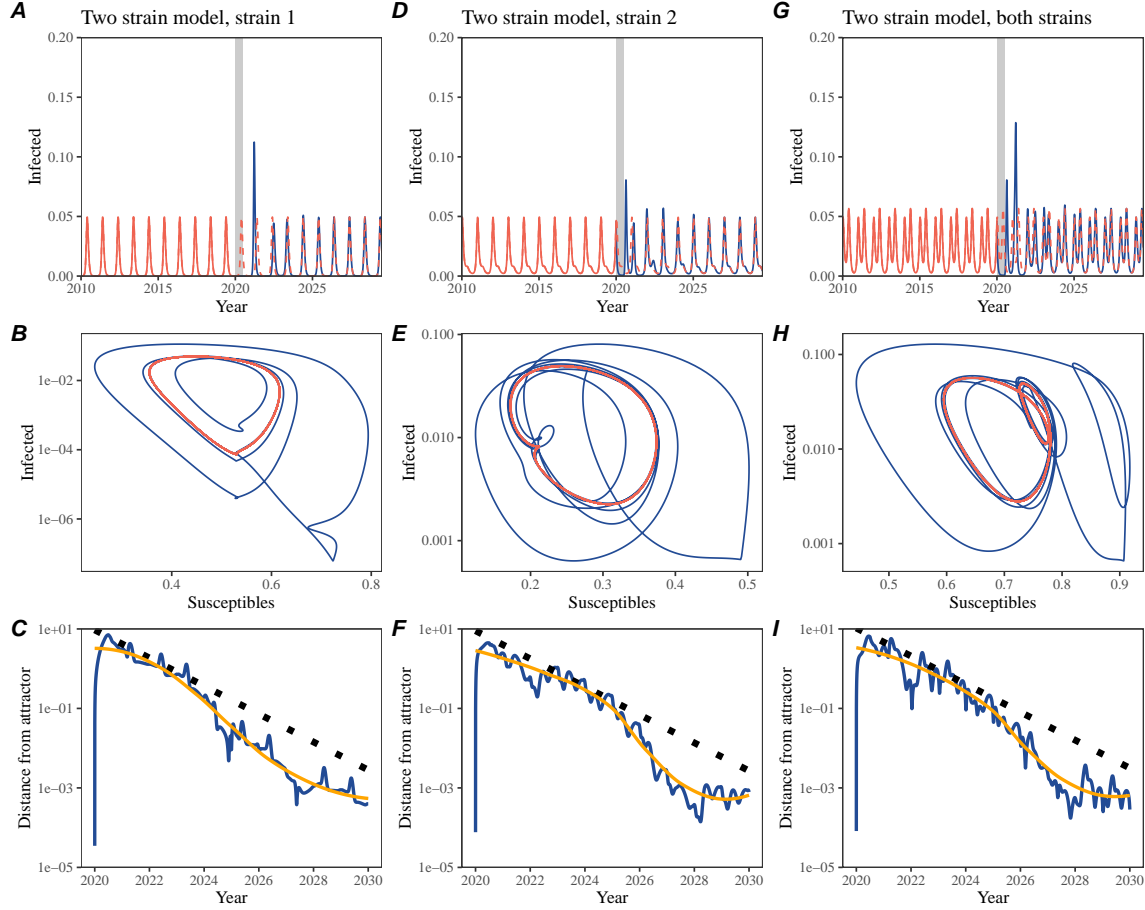


Figure S3: A simple method to measure pathogen resilience following pandemic perturbations for a two-strain competition system with seasonal forcing. (A, D, G) Simulated epidemic trajectories using a two-strain system with seasonal forcing (amplitude of 0.2). In this model, two strains compete through cross immunity. Red and blue solid lines represent epidemic dynamics before and after interventions are introduced, respectively. Red dashed lines represent counterfactual epidemic dynamics in the absence of interventions. Gray regions indicate the duration of interventions. (B, E, H) Phase plane representation of the time series in panels A, D, and G alongside the corresponding susceptible host dynamics. Red and blue solid lines represent epidemic trajectories on an SI phase plane before and after interventions are introduced, respectively. (C, F, I) Changes in logged distance from the attractor over time. Blue lines represent the logged distance from the attractor. Orange lines represent the locally estimated scatterplot smoothing (LOESS) fits to the logged distance from the attractor. Dotted lines show the intrinsic resilience of the seasonally unforced system.

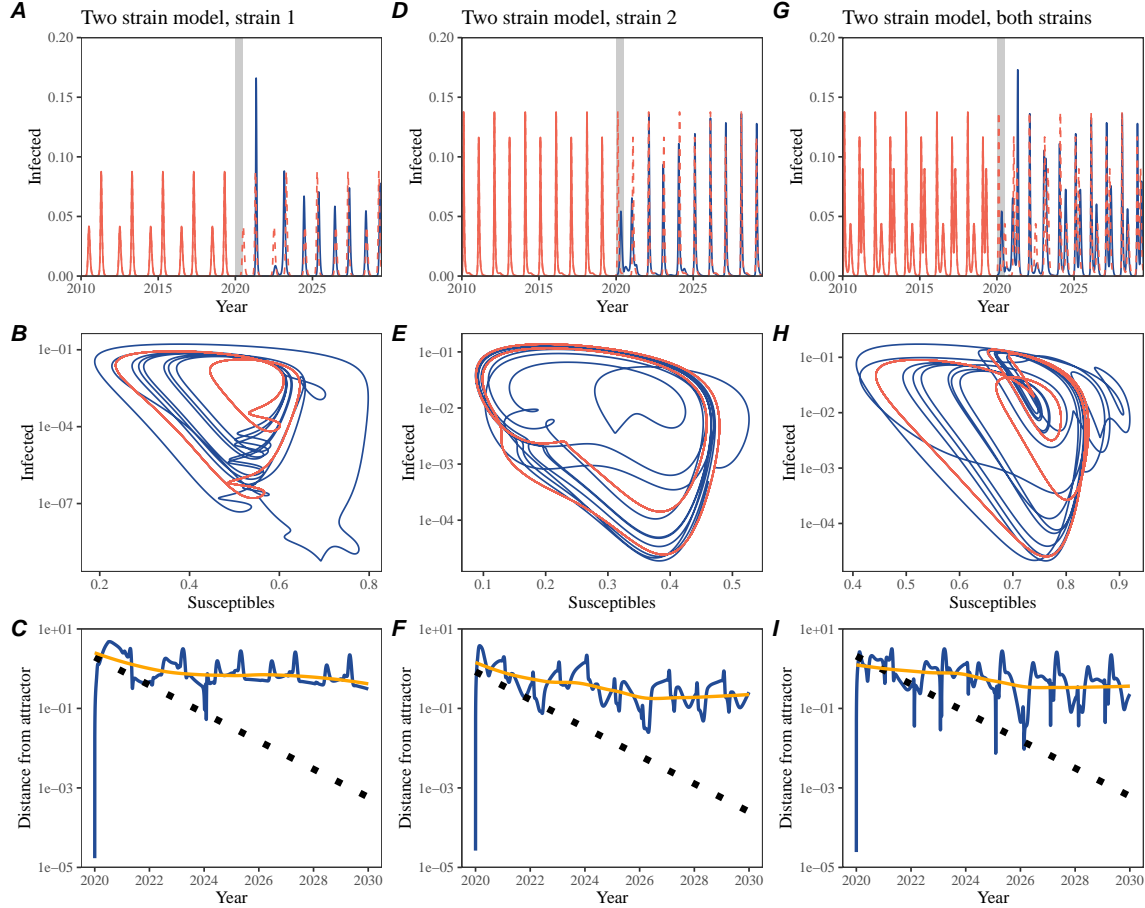


Figure S4: A simple method to measure pathogen resilience following pandemic perturbations for a multi-strain competition system with strong seasonal forcing. (A, D, G) Simulated epidemic trajectories using a two-strain system with seasonal forcing (amplitude of 0.2). In this model, two strains compete through cross immunity. Red and blue solid lines represent epidemic dynamics before and after interventions are introduced, respectively. Red dashed lines represent counterfactual epidemic dynamics in the absence of interventions. Gray regions indicate the duration of interventions. (B, E, H) Phase plane representation of the time series in panels A, D, and G alongside the corresponding susceptible host dynamics. Red and blue solid lines represent epidemic trajectories on an SI phase plane before and after interventions are introduced, respectively. (C, F, I) Changes in logged distance from the attractor over time. Blue lines represent the logged distance from the attractor. Orange lines represent the locally estimated scatterplot smoothing (LOESS) fits to the logged distance from the attractor. Dotted lines show the intrinsic resilience of the seasonally unforced system.

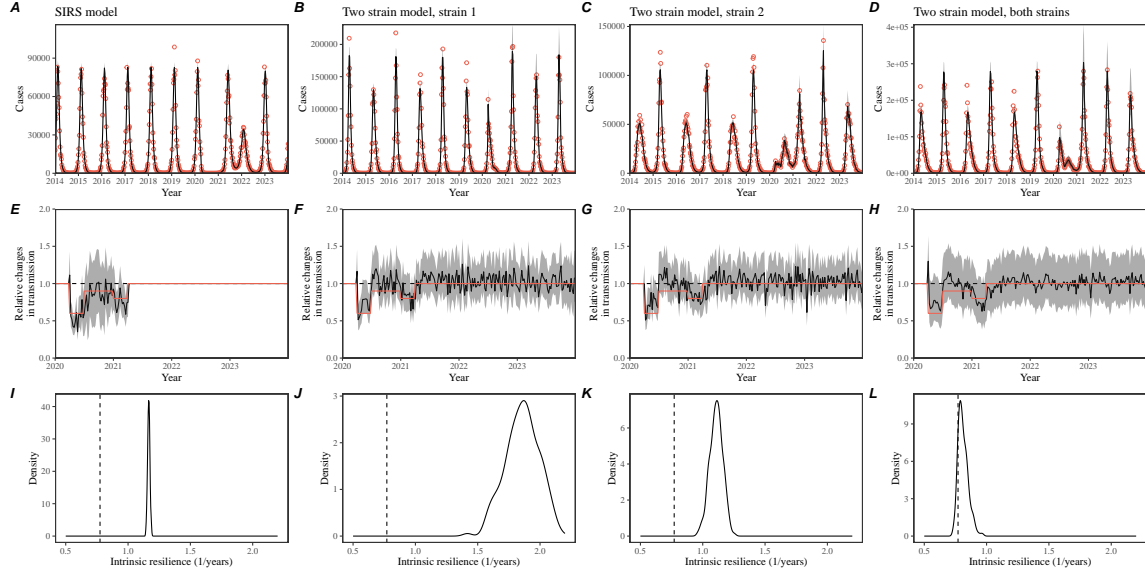


Figure S5: Mechanistic model fits to simulated data and inferred intrinsic resilience. We simulated discrete time, stochastic epidemic trajectories using a seasonally forced SIRS model (A,E,I) and a seasonally forced two-strain model (B–D, F–H, and J–L) and tested whether we can estimate the intrinsic resilience of the seasonally unforced versions of the model by fitting a mechanistic model (Supplementary Text). We fitted the same discrete time, one strain, deterministic SIRS model in each scenario. (A–D) Simulated case time series from corresponding models shown in the title (red) and SIRS model fits (black). (E–H) Assumed changes in transmission due to pandemic perturbations (red) and estimated time-varying relative transmission rates for the perturbation impact from the SIRS model fits (black). Solid lines and shaded regions represent fitted posterior median and 95% credible intervals. (I–L) Comparisons between the true and estimated intrinsic resilience of the seasonally unforced system. Vertical lines represent the true intrinsic resilience of the seasonally unforced system. Density plots represent the posterior distribution of the inferred intrinsic resilience of the seasonally unforced SIRS model using fitted parameters.

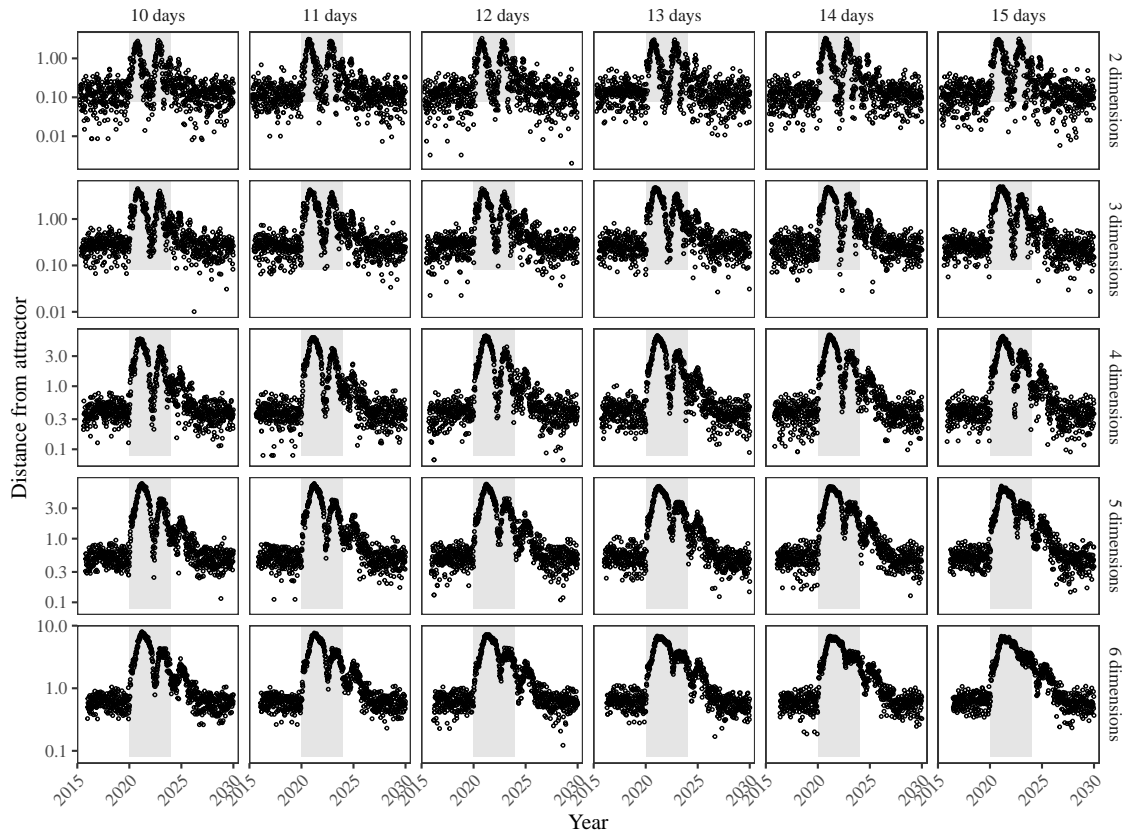


Figure S6: Sensitivity of the distance from the attractor to choice of embedding lags and dimensions. Sensitivity analysis for the distance-from-attractor time series shown in Figure 3E in the main text by varying the embedding lag between 10–15 days and embedding dimensions between 2–6 dimensions. The gray region represents the assumed period of pandemic perturbation.

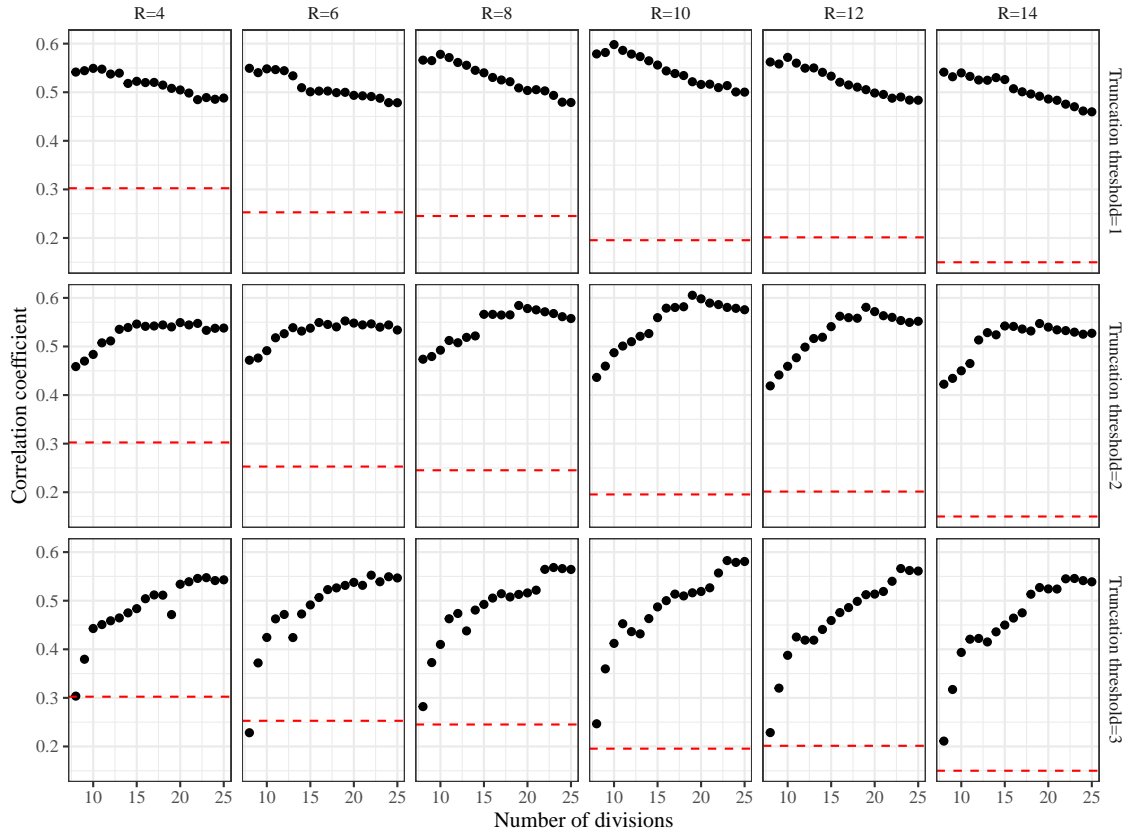


Figure S7: Impact of fitting window selection on the estimation of empirical resilience. We simulated 500 epidemics of a stochastic SIRS model with randomly drawn parameters and randomly generated pandemic perturbations (Supplementary Text). For each simulation, we varied the false nearest neighbor threshold R for reconstructing the empirical attractor as well as the parameters for regression window selection (i.e., the truncation threshold a and the number of divisions K). Each point represents the resulting correlation coefficient between empirical and intrinsic resilience estimates for a given scenario. Dashed lines represent the correlation coefficient between empirical and intrinsic resilience estimates for the naive approach that fits a linear regression on a log scale, starting from the maximum distance until the end of the time series.

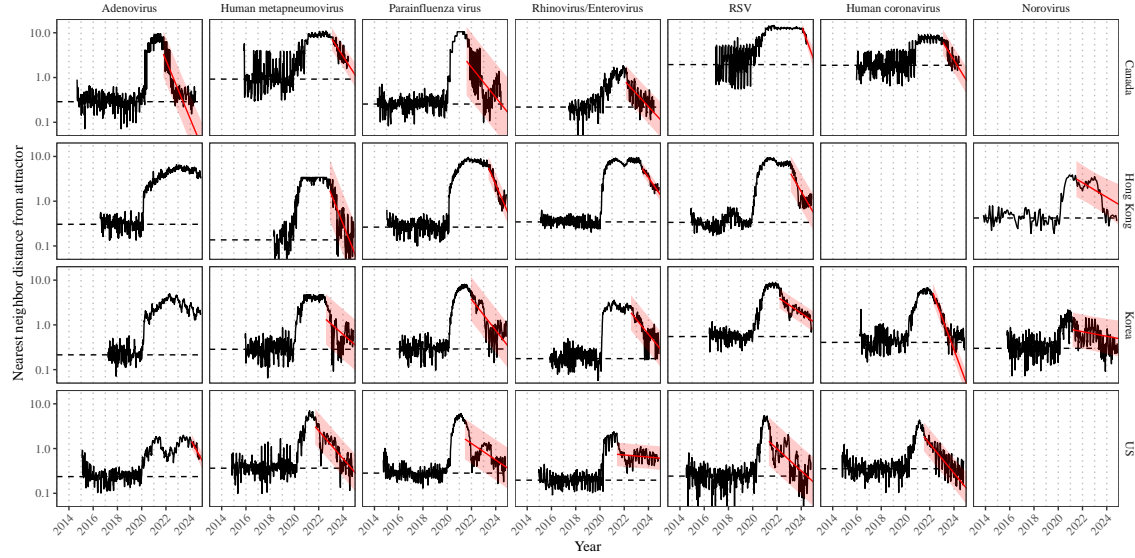


Figure S8: Estimated time series of distance from the attractor for each pathogen and corresponding linear regression fits using automated window selection criteria across Canada, Hong Kong, Korea, and the US. Black lines represent the estimated distance from the attractor. Red lines and shaded regions represent the linear regression fits and corresponding 95% confidence intervals. Dashed lines represent the average of the pre-pandemic nearest neighbor distances.

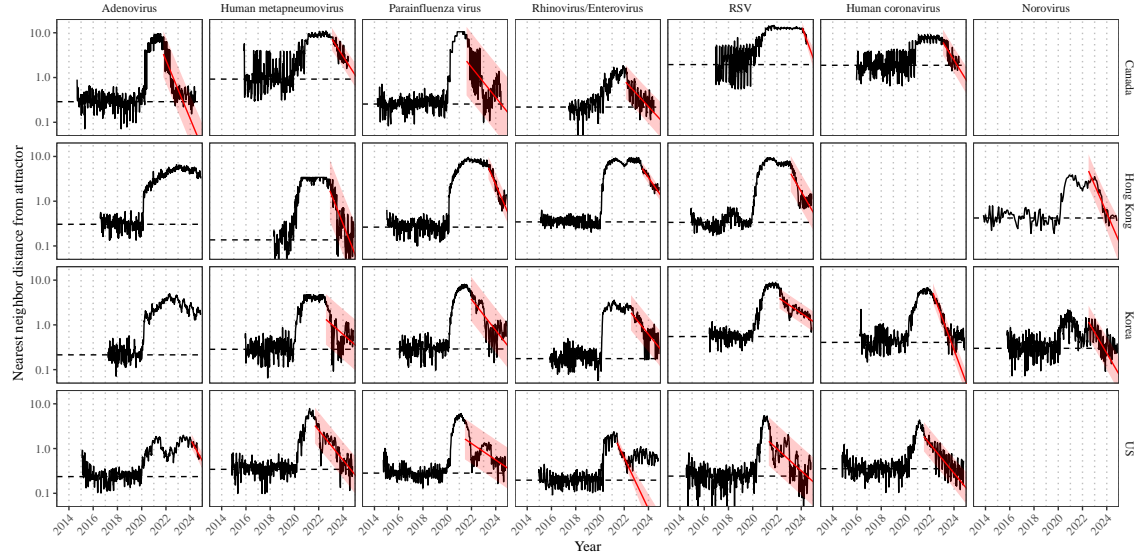


Figure S9: Estimated time series of distance from the attractor for each pathogen and corresponding linear regression fits across Canada, Hong Kong, Korea, and the US, including ad-hoc regression window selection. We used ad-hoc regression windows for norovirus in Hong Kong and Korea and rhinovirus/enterovirus in the US. Black lines represent the estimated distance from the attractor. Red lines and shaded regions represent the linear regression fits and corresponding 95% confidence intervals. Dashed lines represent the average of the pre-pandemic nearest neighbor distances.

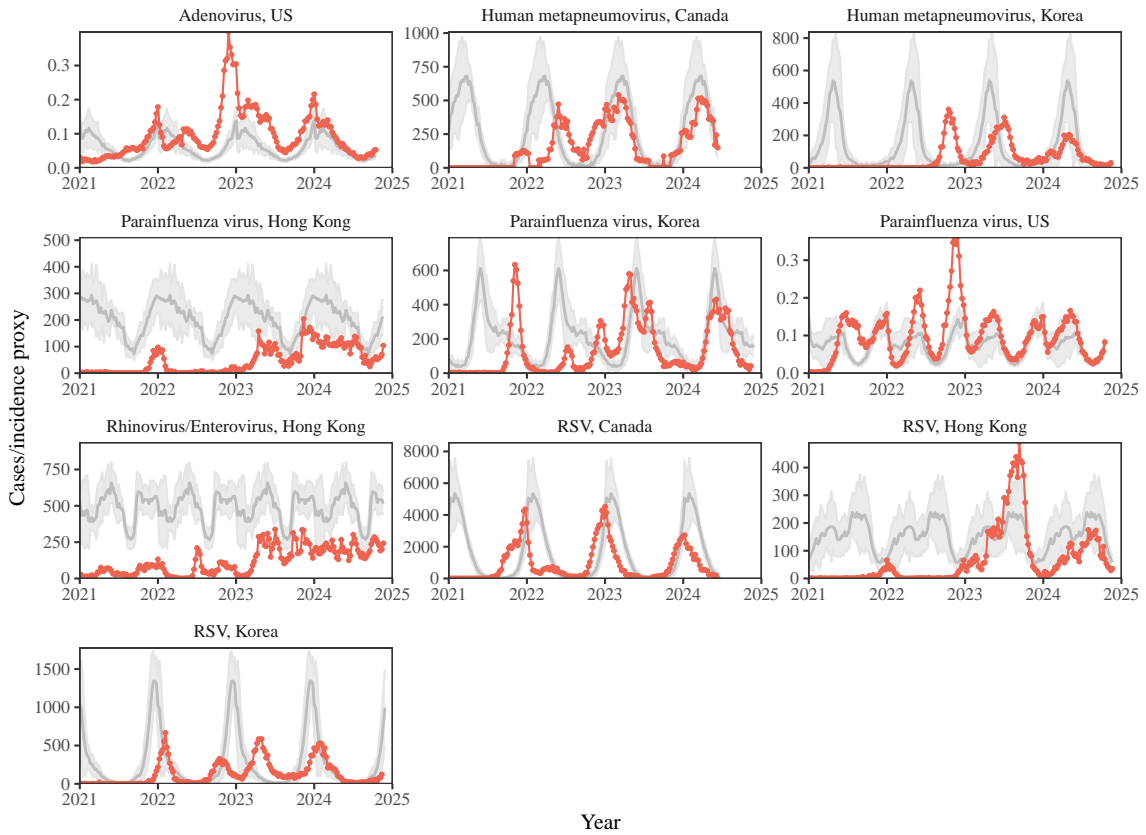


Figure S10: Observed dynamics for pathogen that are predicted to return after the end of 2024. Red points and lines represent data before 2020. Gray lines and shaded regions represent the mean seasonal patterns and corresponding 95% confidence intervals around the mean, previously shown in Figure 1.

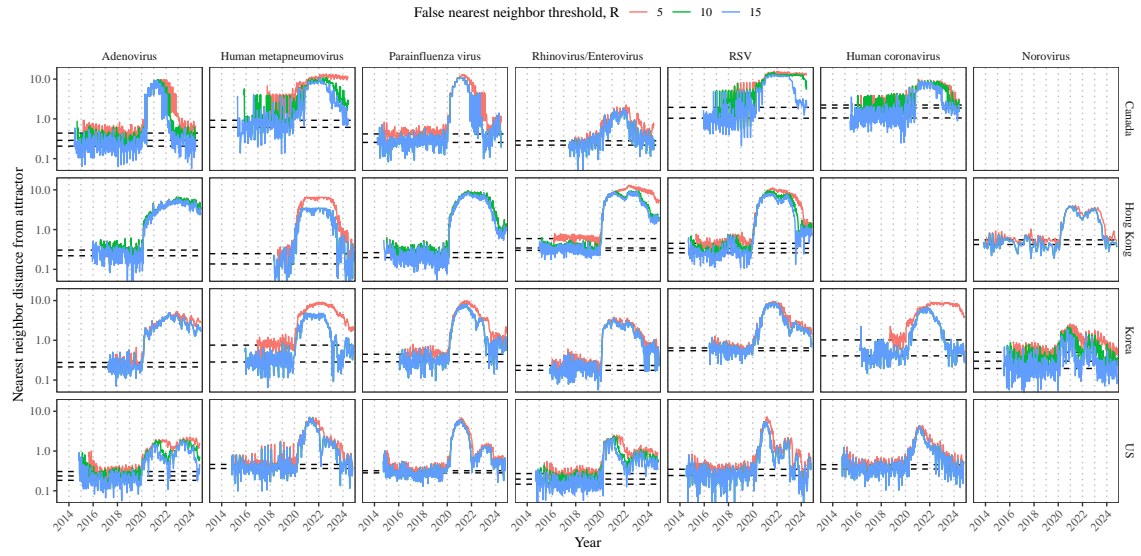


Figure S11: Estimated time series of distance from the attractor for each pathogen across different choices about false nearest neighbor threshold values. Using higher threshold values for the false nearest neighbor approach gives lower embedding dimensions. Colored lines represent the estimated distance from the attractor for different threshold values.

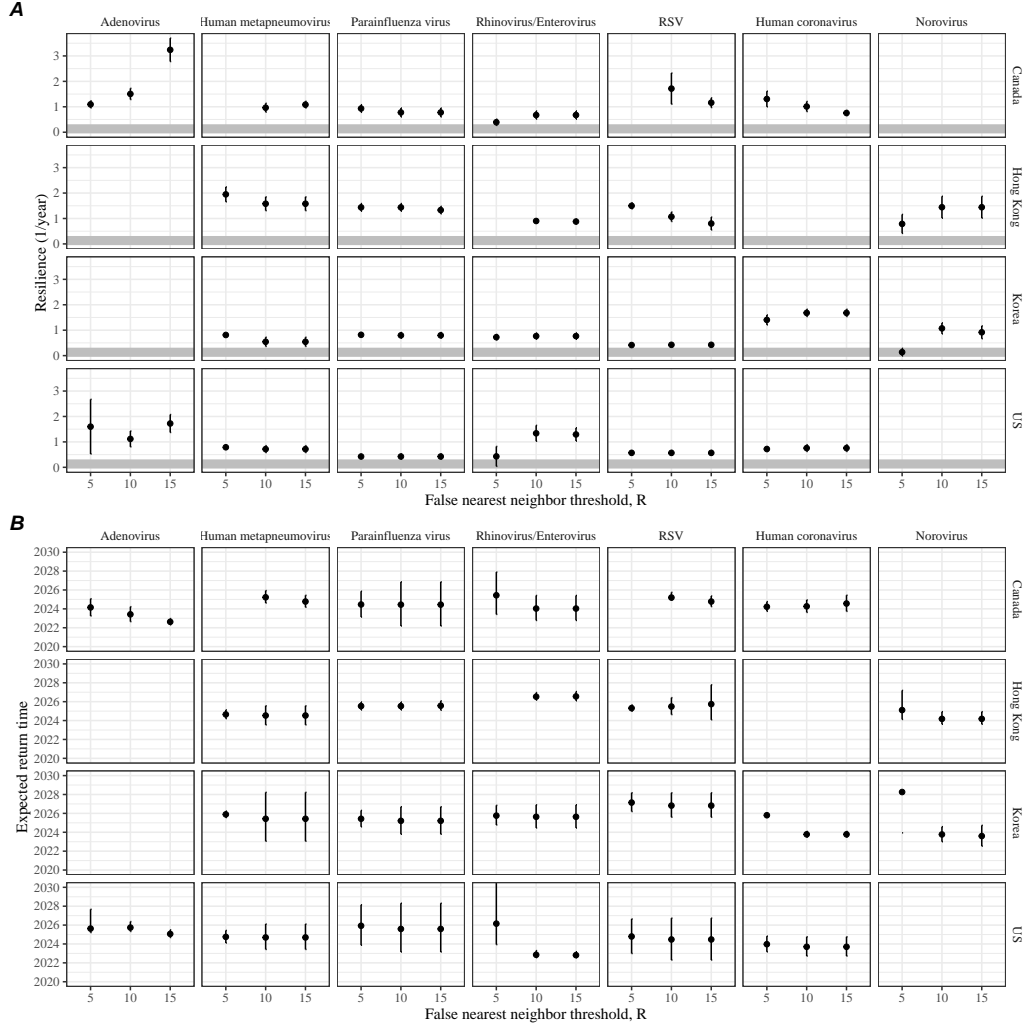


Figure S12: Summary of resilience estimates and predictions for return time across different choices about false nearest neighbor threshold values. The automated window selection method was used for all scenarios to estimate pathogen resilience, except for norovirus in Hong Kong and Korea and rhinovirus/enterovirus in the US. We used the same ad-hoc regression windows for norovirus in Hong Kong and Korea and rhinovirus/enterovirus in the US as we did in the main analysis. (A) Estimated pathogen resilience. The gray horizontal line represents the intrinsic resilience of pre-vaccination measles dynamics. (B) Predicted timing of when each pathogen will return to their pre-pandemic cycles. The dashed line in panel B indicates the end of 2024. Error bars represent 95% confidence intervals.

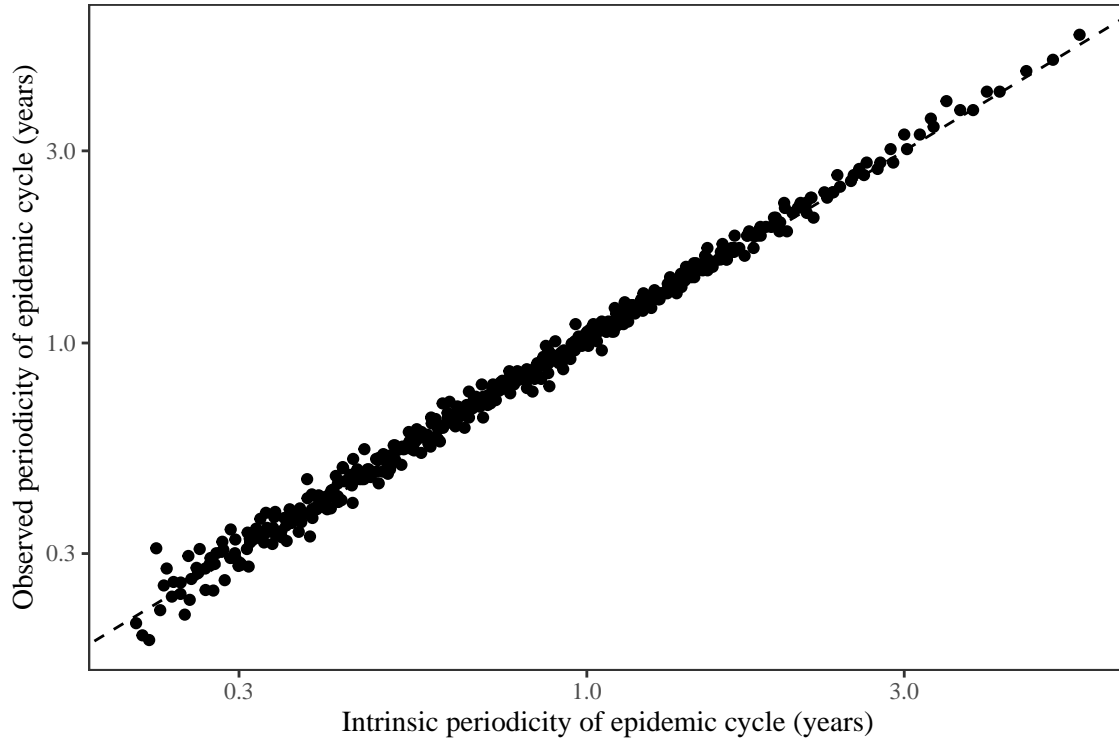


Figure S13: **Comparison between the observed and intrinsic periodicity of the epidemic cycle of the seasonally unforced SIRS model.** The observed periodicity of the epidemic corresponds to the periodicity at which maximum spectral density occurs. The intrinsic periodicity of the epidemic corresponds to $2\pi/\text{Im}(\lambda)$, where $\text{Im}(\lambda)$ is the imaginary part of the eigenvalue.

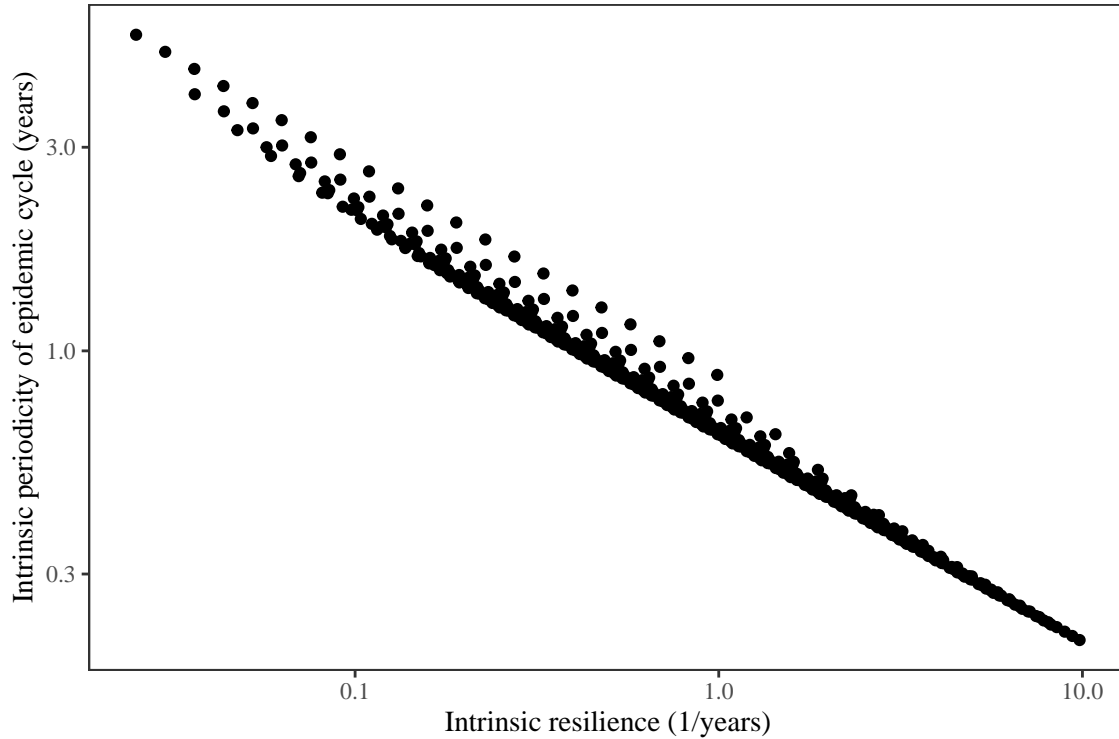


Figure S14: **Comparison between the intrinsic resilience and periodicity of the epidemic cycle of the seasonally unforced SIRS model.** The intrinsic resilience of the epidemic corresponds to the negative of the real value of the eigenvalue $-\text{Re}(\lambda)$. The intrinsic periodicity of the epidemic corresponds to $2\pi/\text{Im}(\lambda)$, where $\text{Im}(\lambda)$ is the imaginary part of the eigenvalue.

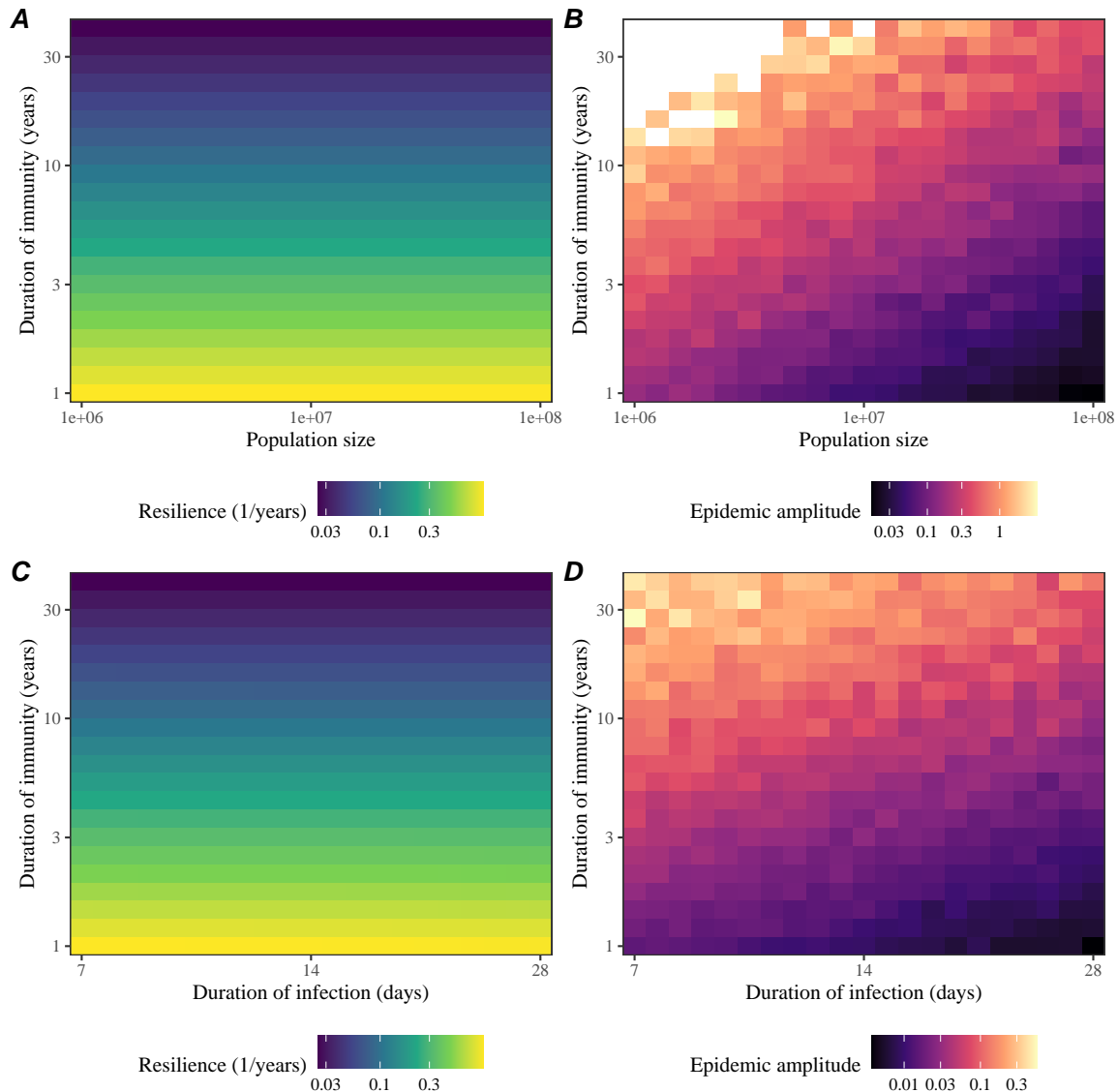


Figure S15: **Impact of population size and the average duration of infection of a host-pathogen system on its sensitivity to stochastic perturbations.** (A) Intrinsic resilience of a system as a function of population size and the average duration of immunity. (B) Epidemic amplitude as a function of population size and the average duration of immunity. (C) Intrinsic resilience of a system as a function of the average duration of infection and immunity. (D) Epidemic amplitude as a function of the average duration of infection and immunity. The epidemic amplitude corresponds to $(\max I - \min I)/(2\bar{I})$, where \bar{I} represents the mean prevalence.

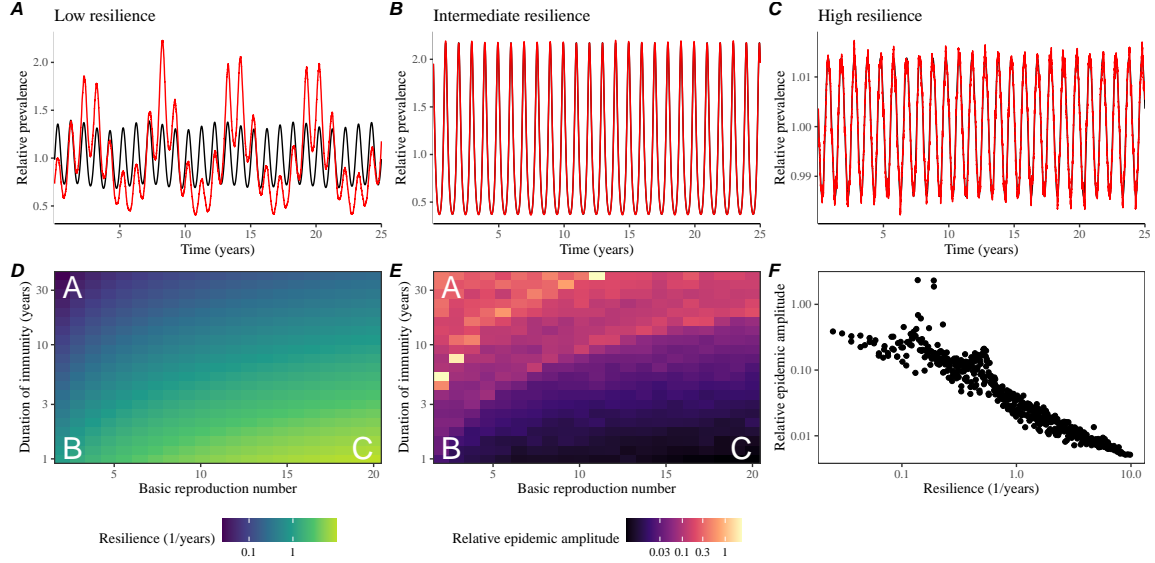


Figure S16: Linking resilience of a host-pathogen system to its sensitivity to stochastic perturbations for the seasonally forced SIRS model. (A–C) Epidemic trajectories of a stochastic SIRS model with demographic stochasticity across three different resilience values: low, intermediate, and high. The relative prevalence was calculated by dividing infection prevalence by its mean value. Black lines represent deterministic epidemic trajectories. Red lines represent stochastic epidemic trajectories. (D) The intrinsic resilience of the seasonally unforced system as a function of the basic reproduction number \mathcal{R}_0 and the duration of immunity. (E) The relative epidemic amplitude, a measure of sensitivity to stochastic perturbations, as a function of the basic reproduction number \mathcal{R}_0 and the duration of immunity. To calculate the relative epidemic amplitude, we first take the relative difference in infection prevalence between stochastic and deterministic trajectories: $\epsilon = (I_{\text{stoch}} - I_{\text{det}})/I_{\text{det}}$. Then, we calculate the difference between maximum and minimum of the relative difference and divide by half: $(\max \epsilon - \min \epsilon)/2$. Labels A–C in panels D and E correspond to scenarios shown in panels A–C. (F) The relationship between pathogen resilience and relative epidemic amplitude.

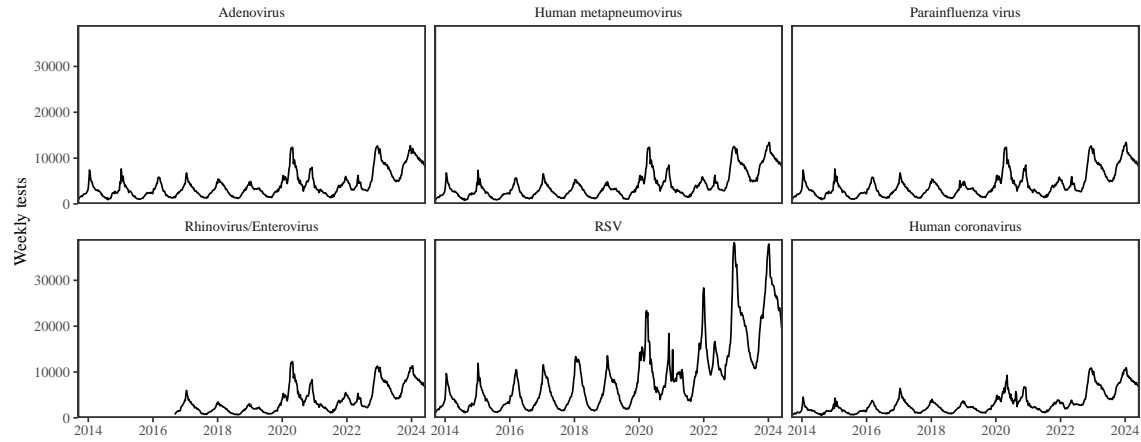


Figure S17: Testing patterns for respiratory pathogens in Canada.

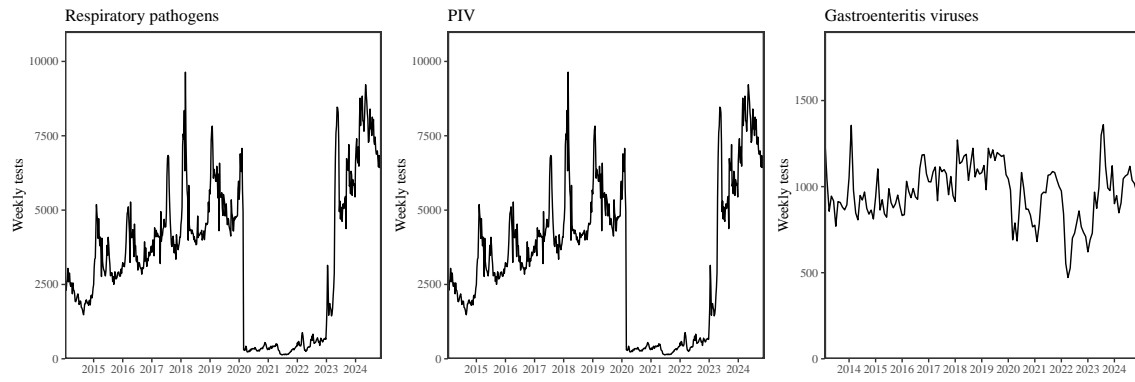


Figure S18: Testing patterns for respiratory pathogens, PIV, and gastroenteritis viruses in Hong Kong.

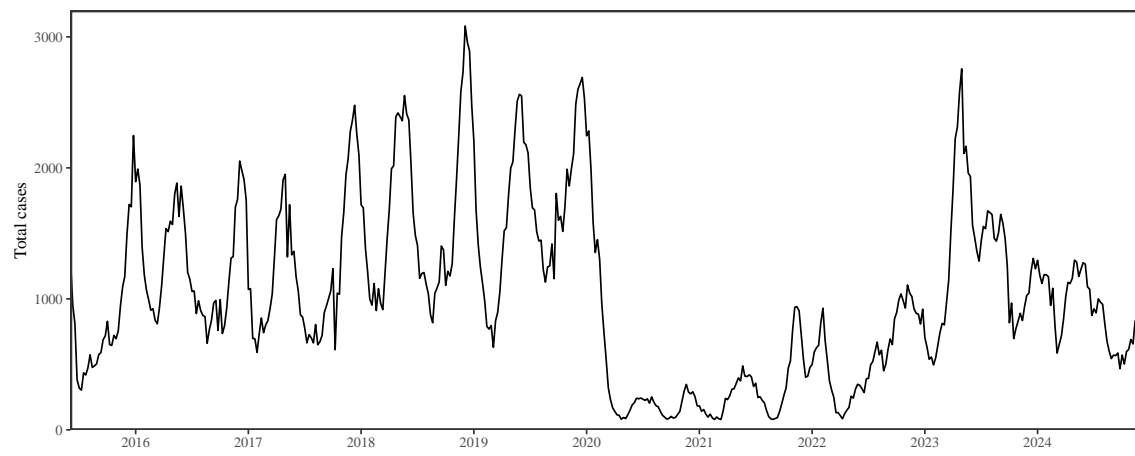


Figure S19: Total number of reported respiratory infection cases in Korea.

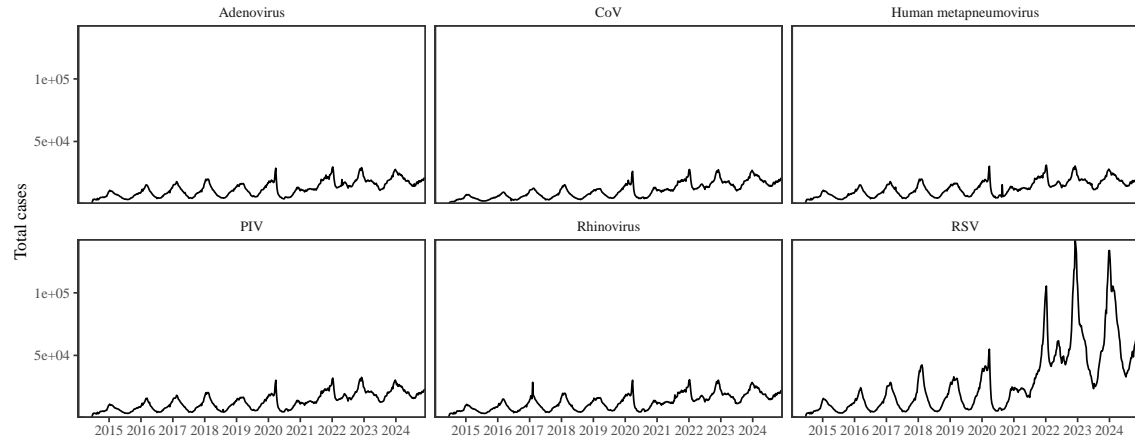


Figure S20: Testing patterns for respiratory pathogens in the US reported through the NREVSS.

838 References

- 839 [1] Rachel E Baker, Sang Woo Park, Wenchang Yang, Gabriel A Vecchi, C Jessica E
840 Metcalf, and Bryan T Grenfell. The impact of COVID-19 nonpharmaceutical
841 interventions on the future dynamics of endemic infections. *Proceedings of the*
842 *National Academy of Sciences*, 117(48):30547–30553, 2020.
- 843 [2] Gabriela B Gomez, Cedric Mahé, and Sandra S Chaves. Uncertain effects of the
844 pandemic on respiratory viruses. *Science*, 372(6546):1043–1044, 2021.
- 845 [3] Mihaly Koltai, Fabienne Krauer, David Hodgson, Edwin van Leeuwen, Marina
846 Treskova-Schwarzbach, Mark Jit, and Stefan Flasche. Determinants of RSV
847 epidemiology following suppression through pandemic contact restrictions. *Epi-*
848 *demics*, 40:100614, 2022.
- 849 [4] Sang Woo Park, Brooklyn Noble, Emily Howerton, Bjarke F Nielsen, Sarah
850 Lentz, Lilliam Ambroggio, Samuel Dominguez, Kevin Messacar, and Bryan T
851 Grenfell. Predicting the impact of non-pharmaceutical interventions against
852 COVID-19 on *Mycoplasma pneumoniae* in the United States. *Epidemics*,
853 49:100808, 2024.
- 854 [5] Amanda C Perofsky, Chelsea L Hansen, Roy Burstein, Shanda Boyle, Robin
855 Prentice, Cooper Marshall, David Reinhart, Ben Capodanno, Melissa Truong,
856 Kristen Schwabe-Fry, et al. Impacts of human mobility on the citywide trans-
857 mission dynamics of 18 respiratory viruses in pre-and post-COVID-19 pandemic
858 years. *Nature communications*, 15(1):4164, 2024.
- 859 [6] Eric J Chow, Timothy M Uyeki, and Helen Y Chu. The effects of the COVID-19
860 pandemic on community respiratory virus activity. *Nature Reviews Microbiol-*
861 *ogy*, 21(3):195–210, 2023.
- 862 [7] Stephen M Kissler, Christine Tedijanto, Edward Goldstein, Yonatan H Grad,
863 and Marc Lipsitch. Projecting the transmission dynamics of SARS-CoV-2
864 through the postpandemic period. *Science*, 368(6493):860–868, 2020.
- 865 [8] Rachel E Baker, Chadi M Saad-Roy, Sang Woo Park, Jeremy Farrar, C Jessica E
866 Metcalf, and Bryan T Grenfell. Long-term benefits of nonpharmaceutical inter-
867 ventions for endemic infections are shaped by respiratory pathogen dynamics.
868 *Proceedings of the National Academy of Sciences*, 119(49):e2208895119, 2022.
- 869 [9] Maaike C Swets, Clark D Russell, Ewen M Harrison, Annemarie B Docherty,
870 Nazir Lone, Michelle Girvan, Hayley E Hardwick, Leonardus G Visser, Pe-
871 ter JM Openshaw, Geert H Groeneveld, et al. SARS-CoV-2 co-infection with
872 influenza viruses, respiratory syncytial virus, or adenoviruses. *The Lancet*,
873 399(10334):1463–1464, 2022.

- 874 [10] Chun-Yang Lin, Joshua Wolf, David C Brice, Yilun Sun, Macauley Locke,
875 Sean Cherry, Ashley H Castellaw, Marie Wehenkel, Jeremy Chase Crawford,
876 Veronika I Zarnitsyna, et al. Pre-existing humoral immunity to human common
877 cold coronaviruses negatively impacts the protective SARS-CoV-2 antibody re-
878 sponse. *Cell host & microbe*, 30(1):83–96, 2022.
- 879 [11] Sam M Murray, Azim M Ansari, John Frater, Paul Klenerman, Susanna
880 Dunachie, Eleanor Barnes, and Ane Ogbe. The impact of pre-existing cross-
881 reactive immunity on SARS-CoV-2 infection and vaccine responses. *Nature*
882 *Reviews Immunology*, 23(5):304–316, 2023.
- 883 [12] John-Sebastian Eden, Chisha Sikazwe, Ruopeng Xie, Yi-Mo Deng, Sheena G
884 Sullivan, Alice Michie, Avram Levy, Elena Cutmore, Christopher C Blyth,
885 Philip N Britton, et al. Off-season RSV epidemics in Australia after easing
886 of COVID-19 restrictions. *Nature communications*, 13(1):2884, 2022.
- 887 [13] Stuart L Pimm. The structure of food webs. *Theoretical population biology*,
888 16(2):144–158, 1979.
- 889 [14] Michael G Neubert and Hal Caswell. Alternatives to resilience for measuring
890 the responses of ecological systems to perturbations. *Ecology*, 78(3):653–665,
891 1997.
- 892 [15] Lance H Gunderson. Ecological resilience—in theory and application. *Annual*
893 *review of ecology and systematics*, 31(1):425–439, 2000.
- 894 [16] Vasilis Dakos and Sonia Kéfi. Ecological resilience: what to measure and how.
895 *Environmental Research Letters*, 17(4):043003, 2022.
- 896 [17] Floris Takens. Detecting strange attractors in turbulence. In *Dynamical Sys-*
897 *tems and Turbulence, Warwick 1980: proceedings of a symposium held at the*
898 *University of Warwick 1979/80*, pages 366–381. Springer, 2006.
- 899 [18] Jonathan Dushoff, Joshua B Plotkin, Simon A Levin, and David JD Earn.
900 Dynamical resonance can account for seasonality of influenza epidemics. *Pro-*
901 , 101(48):16915–16916, 2004.
- 902 [19] Alan Hastings, Carole L Hom, Stephen Ellner, Peter Turchin, and H Charles J
903 Godfray. Chaos in ecology: is mother nature a strange attractor? *Annual review*
904 *of ecology and systematics*, pages 1–33, 1993.
- 905 [20] Alan Hastings, Karen C Abbott, Kim Cuddington, Tessa Francis, Gabriel Gell-
906 ner, Ying-Cheng Lai, Andrew Morozov, Sergei Petrovskii, Katherine Scran-
907 ton, and Mary Lou Zeeman. Transient phenomena in ecology. *Science*,
908 361(6406):eaat6412, 2018.

- 909 [21] Matthew B Kennel, Reggie Brown, and Henry DI Abarbanel. Determining
910 embedding dimension for phase-space reconstruction using a geometrical con-
911 struction. *Physical review A*, 45(6):3403, 1992.
- 912 [22] Eugene Tan, Shannon Algar, Débora Corrêa, Michael Small, Thomas Stemler,
913 and David Walker. Selecting embedding delays: An overview of embedding
914 techniques and a new method using persistent homology. *Chaos: An Interdis-*
915 *ciplinary Journal of Nonlinear Science*, 33(3), 2023.
- 916 [23] Bjarke Frost Nielsen, Sang Woo Park, Emily Howerton, Olivia Frost Lorentzen,
917 Mogens H Jensen, and Bryan T Grenfell. Complex multiannual cycles of My-
918 coplasma pneumoniae: persistence and the role of stochasticity. *arXiv*, 2025.
- 919 [24] Samantha Bosis, Susanna Esposito, HGM Niesters, GV Zuccotti, G Marseglia,
920 Marcello Lanari, Giovanna Zuin, C Pelucchi, ADME Osterhaus, and Nicola
921 Principi. Role of respiratory pathogens in infants hospitalized for a first episode
922 of wheezing and their impact on recurrences. *Clinical microbiology and infection*,
923 14(7):677–684, 2008.
- 924 [25] Miguel L O’Ryan, Yalda Lucero, Valeria Prado, María Elena Santolaya, Marcela
925 Rabello, Yanahara Solis, Daniela Berriós, Miguel A O’Ryan-Soriano, Hector
926 Cortés, and Nora Mamani. Symptomatic and asymptomatic rotavirus and
927 norovirus infections during infancy in a Chilean birth cohort. *The Pediatric
928 infectious disease journal*, 28(10):879–884, 2009.
- 929 [26] Virginia E Pitzer, Cécile Viboud, Vladimir J Alonso, Tanya Wilcox, C Jessica
930 Metcalf, Claudia A Steiner, Amber K Haynes, and Bryan T Grenfell. Environmental
931 drivers of the spatiotemporal dynamics of respiratory syncytial virus in
932 the United States. *PLoS pathogens*, 11(1):e1004591, 2015.
- 933 [27] Arthur WD Edridge, Joanna Kaczorowska, Alexis CR Hoste, Margreet Bakker,
934 Michelle Klein, Katherine Loens, Maarten F Jebbink, Amy Matser, Cormac M
935 Kinsella, Paloma Rueda, et al. Seasonal coronavirus protective immunity is
936 short-lasting. *Nature medicine*, 26(11):1691–1693, 2020.
- 937 [28] Jennifer M Radin, Anthony W Hawksworth, Peter E Kammerer, Melinda Bal-
938 ansay, Rema Raman, Suzanne P Lindsay, and Gary T Brice. Epidemiology
939 of pathogen-specific respiratory infections among three US populations. *PLoS
940 One*, 9(12):e114871, 2014.
- 941 [29] Guojian Lv, Limei Shi, Yi Liu, Xuecheng Sun, and Kai Mu. Epidemiological
942 characteristics of common respiratory pathogens in children. *Scientific Reports*,
943 14(1):16299, 2024.
- 944 [30] Saverio Caini, Adam Meijer, Marta C Nunes, Laetitia Henaff, Malaika Zounon,
945 Bronke Boudewijns, Marco Del Riccio, and John Paget. Probable extinction of

- 946 influenza b/yamagata and its public health implications: a systematic literature
947 review and assessment of global surveillance databases. *The Lancet Microbe*,
948 2024.
- 949 [31] Zhiyuan Chen, Joseph L-H Tsui, Bernardo Gutierrez, Simon Busch Moreno,
950 Louis du Plessis, Xiaowei Deng, Jun Cai, Sumali Bajaj, Marc A Suchard,
951 Oliver G Pybus, et al. COVID-19 pandemic interventions reshaped the global
952 dispersal of seasonal influenza viruses. *Science*, 386(6722):eadq3003, 2024.
- 953 [32] Hai Nguyen-Tran, Sang Woo Park, Kevin Messacar, Samuel R Dominguez,
954 Matthew R Vogt, Sallie Permar, Perdita Permaul, Michelle Hernandez, Daniel C
955 Douek, Adrian B McDermott, et al. Enterovirus D68: a test case for the use of
956 immunological surveillance to develop tools to mitigate the pandemic potential
957 of emerging pathogens. *The Lancet Microbe*, 3(2):e83–e85, 2022.
- 958 [33] Bryan T Grenfell, Ottar N Bjørnstad, and Bärbel F Finkenstädt. Dynamics of
959 measles epidemics: scaling noise, determinism, and predictability with the TSIR
960 model. *Ecological monographs*, 72(2):185–202, 2002.
- 961 [34] Samit Bhattacharyya, Per H Gesteland, Kent Korgenski, Ottar N Bjørnstad,
962 and Frederick R Adler. Cross-immunity between strains explains the dynamical
963 pattern of paramyxoviruses. *Proceedings of the National Academy of Sciences*,
964 112(43):13396–13400, 2015.
- 965 [35] Katharine R Dean, Fabienne Krauer, Lars Walløe, Ole Christian Lingjærde, Bar-
966 Barbara Bramanti, Nils Chr Stenseth, and Boris V Schmid. Human ectoparasites
967 and the spread of plague in Europe during the Second Pandemic. *Proceedings
968 of the National Academy of Sciences*, 115(6):1304–1309, 2018.
- 969 [36] Margarita Pons-Salort and Nicholas C Grassly. Serotype-specific immunity
970 explains the incidence of diseases caused by human enteroviruses. *Science*,
971 361(6404):800–803, 2018.
- 972 [37] Sarah Cobey and Edward B Baskerville. Limits to causal inference with state-
973 space reconstruction for infectious disease. *PloS one*, 11(12):e0169050, 2016.
- 974 [38] P Rohani, CJ Green, NB Mantilla-Beniers, and Bryan T Grenfell. Ecological
975 interference between fatal diseases. *Nature*, 422(6934):885–888, 2003.
- 976 [39] Sema Nickbakhsh, Colette Mair, Louise Matthews, Richard Reeve, Paul CD
977 Johnson, Fiona Thorburn, Beatrix Von Wissmann, Arlene Reynolds, James
978 McMenamin, Rory N Gunson, et al. Virus–virus interactions impact the popu-
979 lation dynamics of influenza and the common cold. *Proceedings of the National
980 Academy of Sciences*, 116(52):27142–27150, 2019.

- 981 [40] Neil Ferguson, Roy Anderson, and Sunetra Gupta. The effect of antibody-
982 dependent enhancement on the transmission dynamics and persistence of
983 multiple-strain pathogens. *Proceedings of the National Academy of Sciences*,
984 96(2):790–794, 1999.
- 985 [41] Public Health Agency of Canada. Respiratory virus detections in
986 Canada. 2024. <https://www.canada.ca/en/public-health/services/surveillance/respiratory-virus-detections-canada.html>. Accessed Sep
987 4, 2024.
- 988 [42] Centre for Health Protection. Detection of pathogens from respiratory spec-
989 imens. 2024. <https://www.chp.gov.hk/en/statistics/data/10/641/642/2274.html>. Accessed Nov 20, 2024.
- 990 [43] Centre for Health Protection. Detection of gastroenteritis viruses from faecal
991 specimens. 2024. <https://www.chp.gov.hk/en/statistics/data/10/641/717/3957.html>. Accessed Nov 20, 2024.
- 992 [44] Korea Disease Control and Prevention Agency. Acute respiratory infection,
993 Sentinel surveillance infectious diseases. 2024. <https://dportal.kdca.go.kr/pot/is/st/ari.do>. Accessed Nov 20, 2024.
- 994 [45] Edward Goldstein, Sarah Cobey, Saki Takahashi, Joel C Miller, and Marc Lipsitch. Predicting the epidemic sizes of influenza A/H1N1, A/H3N2, and B: a statistical method. *PLoS medicine*, 8(7):e1001051, 2011.
- 995 [46] Karline Soetaert, Thomas Petzoldt, and R Woodrow Setzer. Solving differential
996 equations in R: package deSolve. *Journal of statistical software*, 33:1–25, 2010.
- 997 [47] R Core Team. *R: A Language and Environment for Statistical Computing*. R Foundation for Statistical Computing, Vienna, Austria, 2023.
- 998 [48] Sang Woo Park, Inga Holmdahl, Emily Howerton, Wenchang Yang, Rachel E
999 Baker, Gabriel A Vecchi, Sarah Cobey, C Jessica E Metcalf, and Bryan T Grenfell. Interplay between climate, childhood mixing, and population-level suscep-
1000 tibility explains a sudden shift in RSV seasonality in Japan. *medRxiv*, pages
1001 2025–03, 2025.
- 1002 [49] Bob Carpenter, Andrew Gelman, Matthew D Hoffman, Daniel Lee, Ben
1003 Goodrich, Michael Betancourt, Marcus A Brubaker, Jiqiang Guo, Peter Li,
1004 and Allen Riddell. Stan: A probabilistic programming language. *Journal of
1005 statistical software*, 76, 2017.
- 1006 [50] Stan Development Team. RStan: the R interface to Stan, 2024. R package
1007 version 2.32.6.